Atmos. Chem. Phys. Discuss., doi:10.5194/acp-2017-11, 2017
Manuscript under review for journal Atmos. Chem. Phys.
Published: 3 February 2017

Atmospheric Chemistry and Physics Discussions

An analysis of the September 2015 severe dust event in the Eastern Mediterranean

Philipp Gasch[1], Daniel Rieger[1], Carolin Walter[1], Pavel Khain[2], Yoav Levi[2], and Bernhard Vogel[1]

[1]Karlsruhe Institute of Technology, Institute of Meteorology and Climate Research, Karlsruhe, Germany
[2]Israel Meteorological Service, Bet Dagan, Israel

Correspondence to: Philipp Gasch (philipp.gasch@kit.edu)

Abstract. In September 2015 one of the severest and unusual dust events on record occurred in the Eastern Mediterranean. Surprisingly, state-of-the-art dust transport models were unable to forecast the event. This study details the reasons for the failure of the models to forecast the dust storm and presents simulations of the event at convection permitting resolution with the modelling system ICON-ART. The results allow for an in-depth analysis of the influence of the synoptic situation, the complex interaction of multiple driving atmospheric systems and the mineral dust radiative effect on the dust event. A comparison of the results with observations reveals the quality of the simulation results with respect to structure and timing of the dust transport. The forecast of the dust event is improved decisively. The event is enabled by the unusually early occurrence of an active Red Sea trough situation with an easterly axis over Mesopotamia. The connected sustained organized meso-scale convection produces multiple cold-pool outflows responsible for intense dust emissions. Complexity is added by the interaction with an intense heat low, the land inward penetrating Eastern Mediterranean sea-breeze and the widespread occurrence of super-critical flow conditions and subsequent hydraulic jumps in the vicinity of the Dead Sea Rift Valley. The newly implemented mineral dust radiation interaction leads to systematically more intense and faster propagating cold-pool outflows in the runs including the mineral dust radiation interaction.

1 Introduction

Mineral dust aerosol plays an important role for the environment. The transport of mineral dust within the atmosphere has an effect on physical processes, chemical composition and biological systems on various temporal and spatial scales (Carslaw et al., 2010; Shao et al., 2011a; Boucher et al., 2013). Therefore, a need exists to correctly represent mineral dust and its effects in atmospheric models.

In the Eastern Mediterranean the impact of mineral dust on the environment, human population and traffic is important due to the unique environmental setting and great population density. Dust events in the Eastern Mediterranean (EM) are usually associated with strong south-westerly and southern flows in the region, although events have been reported under easterly flow conditions (Dayan et al., 1991; Levi and Rosenfeld, 1996). As a result, the most important remote dust source regions for the EM are situated in north-western Africa and the southern Arabian peninsula (Ganor, 1991; Kubilay et al., 2000). According to a subjective synoptic classification conducted by Dayan et al. (2008), the synoptic scale systems associated with dust transport

Atmos. Chem. Phys. Discuss., doi:10.5194/acp-2017-11, 2017
Manuscript under review for journal Atmos. Chem. Phys.
Published: 3 February 2017

Atmospheric Chemistry and Physics Discussions

towards the EM are with a frequency of 60% Cyprus Lows, Sharav cyclones with 12% and Red Sea troughs with 12% as well. Consequently, the number of dust events in the EM is correlated with cyclone activity in the region (Kishcha et al., 2016, and references therein). Long-range mineral dust transport towards the EM peaks during the transitional seasons in spring and autumn (Offer and Goossens, 2001), when low pressure systems and their associated fronts occur most frequently in the region (Singer et al., 2003, and references therein; Dayan et al., 2008). Resulting from the climatology of dust events in the EM, many studies investigate and simulate dust events in connection with low pressure systems and long-range transport of mineral dust from the Sahara towards the EM (Vogel et al., 2006; Spyrou et al., 2013; Rémy et al., 2015; Kishcha et al., 2016).

In September 2015 an exceptional dust event occurred in the EM. The impact of the event on the EM region was severe, with five people reported to have died, hundreds hospitalized and daily life as well as traffic in the region disrupted (NASA Earth Observatory, 2015; The Weather Channel, 2015; Times Of Israel, 2015). The event was remarkable with respect to magnitude, timing, duration and dust transport direction. Dust surface concentrations were more than 100 times the normal, exceeding 5000 μg m^{-3} at some stations. The Israeli Meteorological Service stated that it was the first time in 75 years that a dust storm reached Israel in early September and lasted beyond one day (Alpert et al., 2016).

Satellite images for the visible part of the electromagnetic spectrum (VIS) from the Moderate Resolution Imaging Spectroradiometer (MODIS) instrument illustrate the evolution of the dust storm (figure 1). Starting from 06 September 2015 high dust concentrations were observed over Syria. On 07 September the full Mesopotamia region and the northern part of the EM was covered by a thick dust layer. Large amounts of dust were transported into the southern EM region during the following night, consequently covering the complete EM on 08 September 2015. The dust plume remained detectable in the region over the course of the next seven days (Alpert et al., 2016). As discussed above, the propagation direction of the record dust storm into the Eastern Mediterranean from east is very unusual.

Adding to the extraordinariness, state-of-the-art dust transport models were unable to forecast the event as is also noted by Mamouri et al. (2016). In the simulations started at 12 UTC 07 September, none of the models is able to forecast a significant dust concentration in the EM region for 12 UTC 08 September (see World Meteorological Organization dust forecast comparison, http://sds-was.aemet.es). This is despite the fact that some of the models use data assimilation of satellite dust optical depth data. The simulated values of the dust optical depth in the EM are between $0.1 - 0.4$ in the multi-model mean with a standard deviation of $0.1 - 0.2$. The forecast failure is highly problematic due to the severe impact of the event.

From EUMETSAT (European Organisation for the Exploitation of Meteorological Satellites) SEVIRI (Spinning Enhanced Visual and Infrared Imager) satellite observations the development of organized meso-scale convective systems (MCS) which produced cold-pool outflows (CPO) over Mesopotamia is detectable. The CPOs and their interaction with a heat low have been suggested as important drivers for the observed dust emissions by Kerkmann et al. (2015). However, to our knowledge a detailed analysis of the driving atmospheric systems and their interaction has not been published so far.

A number of studies have shown that the inability to represent organized meso-scale convection and the related CPOs in models with parametrized convection can lead to a substantial underestimation of dust emissions (Marsham et al., 2011; Heinold et al., 2013). However, CPOs have been identified as important systems contributing to dust emission (Knippertz et al., 2007; Marsham et al., 2011; Heinold et al., 2013) and their occurrence has been documented for all major dust source regions world-

Atmos. Chem. Phys. Discuss., doi:10.5194/acp-2017-11, 2017
Manuscript under review for journal Atmos. Chem. Phys.
Published: 3 February 2017

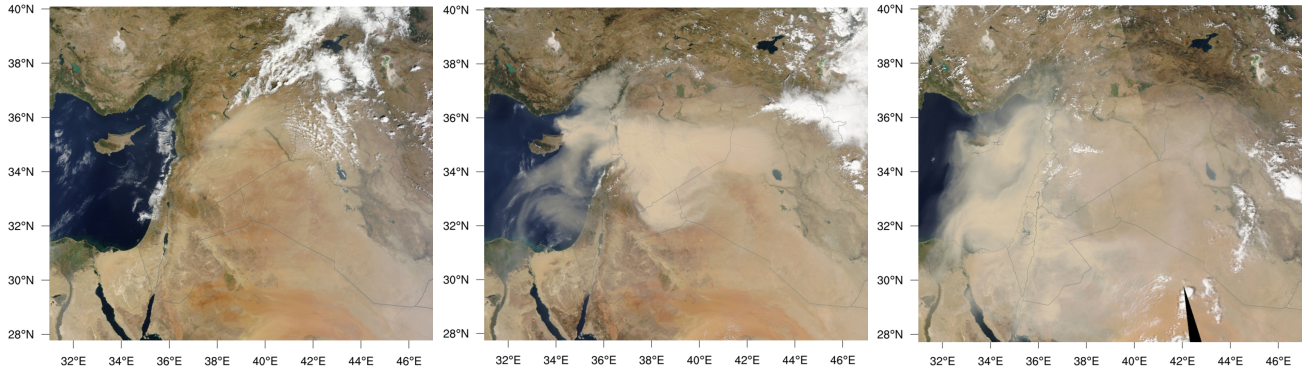

Figure 1. MODIS VIS satellite images of the EM region, from left to right for 06, 07 and 08 September 2015 (NASA Worldview, 2016).

wide (Knippertz, 2014). Therefore, the existence of CPOs detectable in satellite observations is suspected as the main reason for the failure of state-of-the-art dust transport models, as all of them operate at resolutions with fully parametrized convection. In order to overcome this problem the ICON-ART (ICOsahedral Nonhydrostatic - Aerosol and Reactive Trace gases) global modelling system (Zängl et al., 2015; Rieger et al., 2015) is used in this study. It is capable of local grid refinements, in this study the finest nest has a convection permitting grid spacing of 2.5 km. The ART extension (Rieger et al., 2015) allows for on-line simulation of dust processes in ICON. The mineral dust radiation interaction has been implemented in ICON-ART as a part of this study as it has been shown to be of great importance for atmospheric processes (Pérez et al., 2006; Heinold et al., 2008; Bangert et al., 2012; Rémy et al., 2015). The mineral dust radiative effect is calculated on-line based on Mie-calculations and feeds back on atmospheric parameters, which in turn can influence mineral dust processes again. Combining the above topics of dust and its interaction with CPOs and radiation, the influence of the radiative effect of dust contained in CPOs is investigated as a part of this study. The modification of the atmospheric radiation budget by CPOs has been shown to be of importance by Redl et al. (2016). They investigate the influence of the radiative effect of moisture contained in CPOs on boundary layer dynamics. However, a shortcoming of their study is the missing radiative effect of mineral dust, which is often emitted by CPOs in desert regions. This is also a shortcoming in the study of Heinold et al. (2013) who simulate dust emission due to CPOs but do not include the mineral dust radiative effect. Kalenderski and Stenchikov (2016) include and investigate the mineral dust radiative effect in their convection permitting simulation of a CPO in the Red Sea region. However, they do not publish systematic findings on its feedback on the CPO structure.

Consequently, the research questions addressed are as follows: (1) Is the forecast of the dust event improved by running convection permitting simulations? (2) How does the synoptic situation relate to its exceptional character? (3) What are the meteorological drivers responsible for pick-up and long-range transport of mineral dust? (4) How does the mineral dust radiative effect influence the dust event in general and the evolution of the CPOs in particular?

Atmos. Chem. Phys. Discuss., doi:10.5194/acp-2017-11, 2017
Manuscript under review for journal Atmos. Chem. Phys.
Published: 3 February 2017

Atmospheric Chemistry and Physics Discussions

2 Model description

ICON is a non-hydrostatic modelling system developed jointly by the German Weather Service (DWD) and the Max Planck Institute for Meteorology (Zängl et al., 2015). It solves the full three-dimensional non-hydrostatic and compressible Navier-Stokes equations for all domains. Thereby, ICON can serve as a unified global numerical weather prediction model and climate modelling system, enabling seamless prediction from the global to local scale with a unified set of model physics. Its major advantages over previous model generations used at DWD and especially important for atmospheric tracer studies are the exact local mass conservation achieved by solving a prognostic equation for density, and the mass-consistent tracer transport achieved by transporting time-averaged mass fluxes computed from the dynamical core and diagnostic reintegration of the mass continuity equation. ICON allows for flexible local grid refinements (nests) with two-way interactions between the respective grids. Furthermore, it features a better scalability on massively parallel computer architectures. Since January 2015 ICON is used for operational weather forecasting at DWD. The ART module is an extension of ICON developed at the Institute of Meteorology and Climate Research at the Karlsruhe Institute of Technology. An overview of the module is given by Rieger et al. (2015). ART is capable of simulating a variety of aerosol species, e.g. volcanic ash, sea salt and radioactive substances. In addition, atmospheric chemistry processes, e.g. two species of very short-lived bromocarbons, a linearised ozone chemistry and photolysis are also available in ART. For the tracer transport simulations the seamless modelling capabilities of ICON are of crucial importance because inconsistencies in tracer transport and tracer physics at the nest boundaries can be avoided, which is a major problem for other modelling systems.

The size distribution of mineral dust is represented by three modes in ART. For each mode the integral values of specific number and mass are the prognostic variables. The distribution of specific number and mass with particle size during transport is described using log-normal distributions for each mode with the diagnostic median diameter of the mass distribution and constant geometric standard deviation as parameters (Mode A, d = 1.5 μm, $\sigma = 1.7$; Mode B, d = 6.7 μm, $\sigma = 1.6$; Mode C, d = 14.2 μm, $\sigma = 1.5$). The processes which affect mineral dust number and/or mass concentrations in ART are sedimentation, dry deposition and wet deposition due to washout. The scheme used for emission of mineral dust in ART is described in Rieger (2016). It is based on an emission scheme introduced by Vogel et al. (2006). Compared to the original version three improvements were implemented, these are (1) the global availability of soil properties (size distribution, residual soil moisture), (2) accounting for the soil dispersion state, and (3) a tile approach used to account for soil type heterogeneity at coarse resolutions. For the equations used the reader is referred to the work by Rieger (2016). The scheme parametrizes the threshold friction velocity above which dust emission can occur according to Shao and Lu (2000). They base their description on a physical balance between aerodynamic drag and lift causing upward directed forces and cohesion and gravity causing downward directed forces on particles. The effect of surface roughness and soil moisture are accounted for through parametrizations by Raupach et al. (1993) and Fécan et al. (1999) respectively, which modify the threshold friction velocity. The regional distribution of soil types used for dust emission in ART is taken from the Harmonized World Soil Database (HWSD) dataset with a resolution of 30 arc seconds (Nachtergaele and Batjes, 2012). The fraction of erodible soil is determined assuming that certain land use classes from the GlobCover2000 dataset (Arino et al., 2008) contribute to mineral dust emission whereas others do not, with snow

Atmos. Chem. Phys. Discuss., doi:10.5194/acp-2017-11, 2017
Manuscript under review for journal Atmos. Chem. Phys.
Published: 3 February 2017

generally prohibiting emissions. The land use classes which can contribute to emission are regions with sparse vegetation, bare areas, closed to open grass- and shrub-lands, furthermore mosaic forest/grassland and shrub-land. In order to retain the high spatial resolution of the dataset for ART a tile approach is used for calculating dust emissions. The tile approach calculates the overall emission in every grid box as a weighted average of the emissions from different soil types based on their fractional coverage of the grid box. Determination of land use classes is difficult in the Levantine region. It has undergone drastic change in recent years due to on-going conflict (Gleick, 2014), problems in transboundary water management (Voss et al., 2013) and a drought period (Notaro et al., 2015). Therefore, widespread, previously cultivated areas exist which are now available to erosion and known to be efficient dust sources (Solomos et al., 2016). These recent land cover changes are not reflected in the GlobCover2000 land use dataset and can result in underestimation of dust emission.

2.1 Mineral dust radiative effect

As a part of this study the on-line dust radiative effect has been implemented in ICON-ART. It is now possible to include the radiative effect of the current, local dust concentration from ART at every grid point and time step in ICON instead of the previously used dust climatology. Through its feedback on radiative fluxes the dust influences atmospheric state, thereby providing a feedback loop back to dust processes again (Tegen et al., 2006; Heinold et al., 2008; Shao et al., 2011a). The implementation was done for the standard radiation scheme utilized by ICON which is the Rapid Radiative Transfer Model (RRTM) described by Mlawer et al. (1997). In our setup, the RRTM is called every 288 seconds for the finest resolution in ICON.

The ART dust radiation routine is called at every time step at which the RRTM is called by ICON. Situated at the interface between ICON and the RRTM, ART modifies the radiative transfer parameters of the climatological dust distribution. Specifically, at every grid-point and for every level the optical depth, single scattering albedo and asymmetry parameter are calculated from the dust optical properties as a function of the dust mass concentration as detailed in Stanelle et al. (2010). The parameters returned by ART are the combined values from the local ART dust concentration plus the Tegen climatology, the latter being used only for aerosol species not simulated in ART.

In order to include the on-line dust radiative effect by modification of the radiative transfer parameters the dust optical properties have to be determined. The mineral dust optical properties are computed with the help Mie calculations using the complex refractive index of mineral dust (Bohren and Huffman, 1983; Petty, 2006; Wagner et al., 2012). This study therefore assumes sphericity as well as a spatially invariant mineral composition of the mineral dust particles. Although this assumption is generally not fulfilled for single mineral dust particles (Otto et al., 2009; Kahnert et al., 2007), it introduces negligible errors for a population of randomly oriented non-spherical particles if only albedo and flux related quantities are calculated (Mishchenko et al., 1995, 1997). Due to the random orientation a collection of particles scatters light similar to a spherical particle because the individual differences disappear in the angular integration (Tegen and Lacis, 1996). Therefore Mie calculations are able to provide a good representation of scattering even for non-spherical particles. The values of the refractive index used to conduct the Mie calculations are the same ones used by Stanelle et al. (2010) for COSMO-ART and therefore not detailed further.

Atmos. Chem. Phys. Discuss., doi:10.5194/acp-2017-11, 2017
Manuscript under review for journal Atmos. Chem. Phys.
Published: 3 February 2017

Atmospheric Chemistry and Physics Discussions

For the Mie calculations a code developed by Bond et al. (2006) was used, this in turn utilizes a subset developed by Mätzler (2002) for calculation of the Mie scattering coefficients and truncation of the series. The code was adapted to allow for processing of multiple wavelengths and averaging to the RRTM wavebands in a post-processing step.

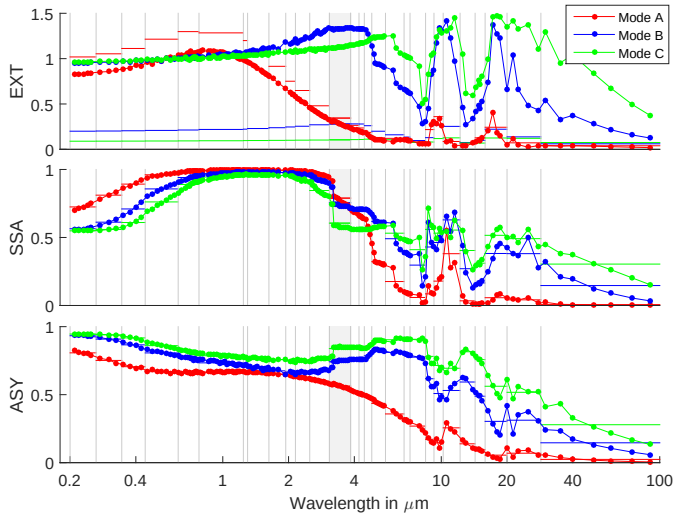

Figure 2. Results from Mie calculations as used by ICON-ART. Points are normalized with respect to value at 550nm, horizontal lines show absolute values. Shown are from top to bottom: Extinction coefficient (EXT) in $m^2\ g^{-1}$, single scattering albedo (SSA) and asymmetry parameter (ASY) for all modes. The borders of the RRTM radiation scheme wavebands are adumbrated as grey lines in the background. The filled grey band represents the waveband present both in the longwave and shortwave part of the RRTM.

The mineral dust optical properties are calculated for three modes and 30 RRTM radiation wavebands, respectively. Results of Mie calculations for the ART mineral dust modes are shown in figure 2 and are comparable to those published by other studies (Tegen and Lacis, 1996; Helmert et al., 2007; Rémy et al., 2015). Although the authors use slightly different size distributions and refractive index properties the results are very similar to the ones presented here.

The optical properties of mineral dust are highly dependent on its particle size distribution represented through three log-normal modes in ART. From the six prognostic variables in ART, the specific dust mass and number concentration for each of the three modes, a median diameter can be diagnosed for each mode. Due to different processes such as sedimentation and dry deposition acting differently on the specific dust mass and number concentrations in ART, the diagnostic median diameter of each mode changes during transport (the standard deviation of each mode is kept constant). In a physical sense, the most important effect is large particles settling out faster due to sedimentation, which results in mostly smaller particles being transported to distant regions within each mode. Therefore, the median diameter of each mode is expected to decrease during transport. Consequently, a new polynomial parametrization of the optical properties per waveband was introduced to account for the change in median diameter during the transport processes. In a post-processing step a third order polynomial is fitted to the results of multiple Mie calculations for median diameters between $0.25 - 1.25$ times the initial median diameter

Atmos. Chem. Phys. Discuss., doi:10.5194/acp-2017-11, 2017
Manuscript under review for journal Atmos. Chem. Phys.
Published: 3 February 2017

Atmospheric Chemistry and Physics Discussions

of the count number distribution. This is done for every mode and every RRTM waveband respectively. The polynomial fit parameters are initialized in ICON-ART and used for determination of optical properties at every grid point with the diagnosed median diameter being the independent variable.

The specifics of the mineral dust radiative effect implementation are available upon request and detailed in Gasch (2016).

2.2 Model set-up

In this study ICON-ART is run in a set-up with one global domain and four nests, with two-way feedback for the meteorological parameters enabled for all domains. Each domain presents a stand-alone model run which obtains its lateral boundary conditions from the coarser domain. For the global domain an R2B6 grid is used, this corresponds to an effective grid spacing of 40 km (Zängl et al., 2015). For every nest, the grid point distance is halved, thereby ending at R2B10 with an effective grid spacing of 2.5 km. The finest domain is circular shaped and centred at $35°$ N, $40°$ E with a radius of approximately 1000 km, thereby containing 507100 grid points. In order to realistically represent organized moist, deep convection a convection permitting model resolution is required. A grid spacing of 2.5 km is generally assumed to be sufficient to permit the development of convection in a non-hydrostatic model. Therefore the convection parametrization, including the parametrization for shallow convection, is switched off for the finest grid.

On the global domain the model consists of 90 levels extending up to the mesosphere, with the lowest level being at 20 m and the highest level at 75 km. For the nests the simulated atmosphere extends into the stratosphere up to 22.5 km containing 60 vertical levels.

For the cloud micro-physical processes a the two-moment cloud scheme is used (Seifert and Beheng, 2006), as this was found to lead to more realistic features of the meso-scale organized convection. The two-moment scheme utilizes a parametrization developed by Seifert and Beheng (2001) which predicts number and mass concentrations for six different hydro-meteor species. These are cloud droplets, rain drops, cloud ice, snow, graupel and hail.

ICON-ART is initialized with analysis fields from the Integrated Forecasting System (IFS) of the European Centre for Medium-Range Weather Forecasts (ECMWF). A limitation with initializing from the IFS analysis datasets is that the IFS has a horizontal grid spacing of approximately 13 km and is therefore non convection-permitting. Thus, when re-initializing ICON-ART with the current meteorological fields any previously existing organized convection is terminated. The IFS initialization data for soil moisture was modified in a region along the Syrian-Iraqi border which showed unrealistically high soil moisture values and spatial patterns without preceding rain or changes in soil properties. Therefore, in a region from $37.5°\text{N} - 41.5°\text{N}$ and $32.5°\text{E} - 35°\text{E}$ the soil moisture index in the four layers provided by the IFS is set to the average value of the region between $36.5°\text{N} - 38°\text{N}$ and $32°\text{E} - 34°\text{E}$ which represents the soil moisture conditions in the region more realistically. The region modified is an important dust source region and emission fluxes for mineral dust increased due to the reduction of the soil moisture content.

The ICON-ART mineral dust dust concentrations are passed on to the next run whenever a reinitialization of the meteorological fields from an IFS analysis is performed. No assimilation of mineral dust concentrations from observations takes place. Hence, the runs are performed as free runs for the mineral dust concentrations with a frequent update of the meteorological

Atmos. Chem. Phys. Discuss., doi:10.5194/acp-2017-11, 2017
Manuscript under review for journal Atmos. Chem. Phys.
Published: 3 February 2017

background conditions from IFS analysis in order to benefit from the data assimilation performed therein. A two week spin-up simulation is performed starting on 23 August 2015 in order to achieve a realistic background concentration for mineral dust on the global domain. Another reinitialization from an IFS analysis is performed at 00 UTC 04 September to obtain a realistic background concentration of mineral dust in the finer domains for the simulations starting at 18 UTC 05 September. From 00 UTC 06 September onwards, a multitude of partially overlapping events take place which need to be simulated correctly in order to obtain a realistic dust distribution in the EM. Therefore, the time chosen for initialization is of crucial importance due to the aforementioned termination of organized convection. Various options were examined, the times chosen for initialization are 18 UTC 05 September and 12 UTC 06 September.

For investigation of the dust radiative effect two simulations are performed. The first is the simulation including the on-line radiation interaction with mineral dust from ART which is called 'ARI' (aerosol radiation interaction) in the following. The second is a simulation in which the mineral dust concentrations are multiplied by zero in the ART routine calculating the radiative effect of dust. This simulation is called 'CTRL' (control) in the following, it contains no mineral dust influence on radiation at all. In this study only the mineral dust radiation interaction is simulated on-line by ART, for all other aerosols the default climatologies are used in all runs.

3 Simulation results and validation

The ICON-ART simulation results show that the dust event consists of multiple stages and is created by the interaction of different meteorological systems. A comparison of model results to available satellite observations highlights the ICON-ART simulation quality.

3.1 Synoptic situation

For the event simulated, the synoptic conditions in the Middle East are distinctively different from the normal summer situation as the ICON-ART model results show. An overview of the modelled synoptic situation is provided in figure 3 at 18 UTC 06 September, as at this point in time all relevant synoptic features are detectable.

The usually dominant Persian trough (Bitan and Sa'Aroni, 1992) does not exist. Instead a low-level synoptic pattern termed Red Sea Trough (RST) with an eastern axis is apparent below 800 hPa which extends northward from the Red Sea towards central Syria under easterly flow conditions. The direction of the trough axis and its position over the Red Sea make it plausible to attribute it to the RST category rather than to the Persian trough category. Furthermore, a characteristic strong southerly flow exists in the Mesopotamia region, which is crucial for the sustained lifetime of the meso-scale organized convection as it advects hot and moist air from the Persian Gulf. The RST is accompanied by a mid-tropospheric trough between $700-400$ hPa extending far southward into the EM under westerly flow conditions. The trough axis runs approximately along the Dead Sea Rift Valley, curving eastwards towards Egypt in the southern part. East of this trough (downstream) high wind speeds up to 20 m s^{-1} exist in a streak running from south-west towards north-east. The streak is situated exactly upstream of the meso-scale convective system (MCS) development region. As suggested in previous studies (Krichak et al., 2012; Vries et al., 2013),

Atmos. Chem. Phys. Discuss., doi:10.5194/acp-2017-11, 2017
Manuscript under review for journal Atmos. Chem. Phys.
Published: 3 February 2017

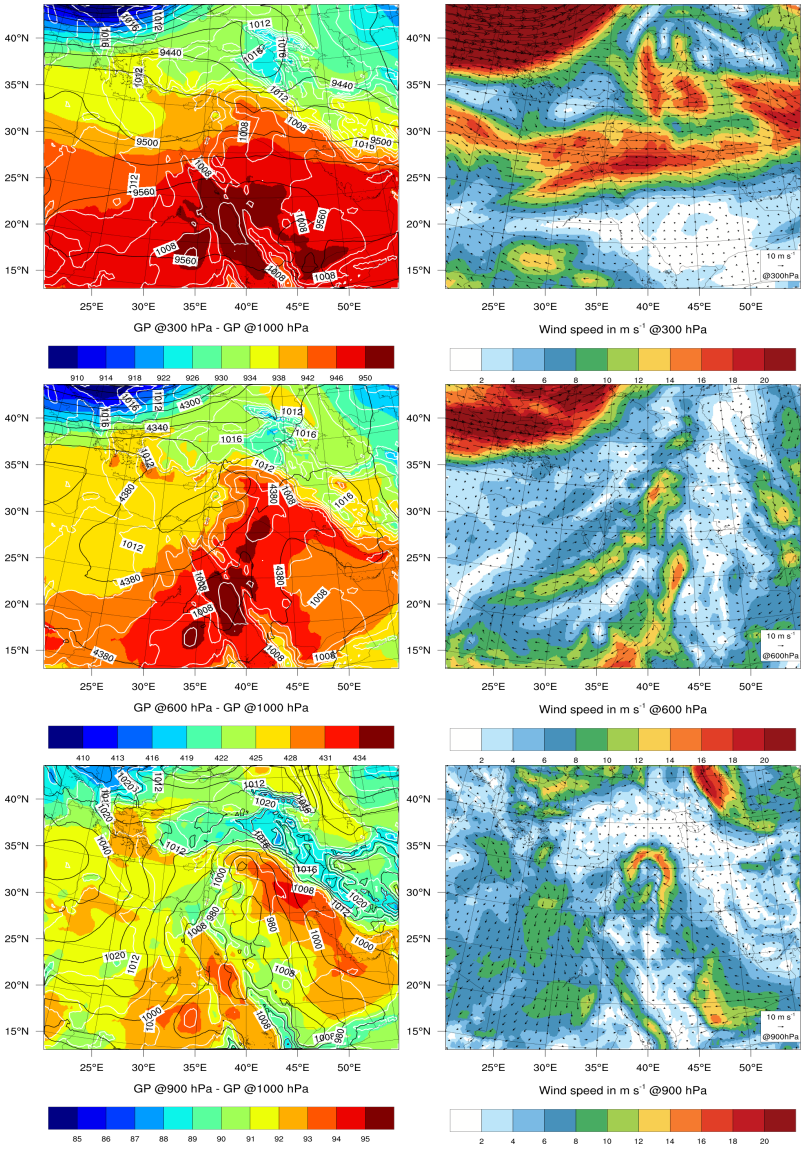

Figure 3. Synoptic situation on 06 September at 18 UTC as simulated by ICON-ART for the global domain. Shown are from top to bottom the 300 hPa, 600 hPa and 900 hPa level. Colour coded on the left side is the relative topography as the geopotential height of the respective layer minus the geopotential height of the 1000 hPa layer. Black lines denote the height of the respective pressure level in geopotential metres at 5 gpm intervals. White lines show surface pressure in hPa. On the right side wind speed is colour coded and wind velocity is shown as vectors.

Atmos. Chem. Phys. Discuss., doi:10.5194/acp-2017-11, 2017
Manuscript under review for journal Atmos. Chem. Phys.
Published: 3 February 2017

Atmospheric Chemistry and Physics Discussions

this marked jet could provide significant moisture transport for the MCS from the Red Sea and Africa in the form of an atmospheric river with high values of atmospheric humidity. At upper tropospheric levels above 400 hPa a short-wave trough exists in the region above Syria. This trough advects positive vorticity and cold air into the region at high altitudes, thereby creating quasi-geostrophic forced ascent and potential instability. In addition, the strong wind-shear between lower and upper levels in the Mesopotamia region produces the conditions necessary for MCSs by enabling a separation of up- and down-draft. In combination with the orographic lifting by the Zagros mountain range, the position of the slowly eastward moving trough enables the development of meso-scale organized convection and determines its position throughout the event. The combination of a low-level RST extending northward and upper tropospheric troughs extending southward into the EM has been termed active RST in previous studies due to its high potential for severe weather (Krichak et al., 2012; Vries et al., 2013). The timing of the active RST synoptic situation is exceptional, as the RST usually starts to occur only by late September or early October (Alpert et al., 2004; Tsvieli and Zangvil, 2005), although events have been documented in August and September (Osetinsky, 2006). The active RST has been linked to severe weather phenomena in the EM and the Arabian peninsula in connection with atmospheric rivers transporting large quantities of precipitable water from eastern Africa, although the specific moisture sources are still debated (Vries et al., 2013, and references therein). The clustering of convectively active days with meso-scale convective organization is often observed during active RST situations (Krichak et al., 2012; Vries et al., 2013). This clustering is also in agreement with a study by Miller et al. (2008), who investigate haboob characteristics in the Arabian peninsula.

As is discussed in Sec. 3.2, the active RST enables the interaction of multiple dust emitting meteorological systems over the course of three days, which explains the extraordinariness of the event with respect to magnitude and spatial extent. The unusual transport direction of the dust plume from Syria and Iraq into the EM from the east is caused by the downstream flank of the RST. To our knowledge, the active RST synoptic situation has previously not been linked to severe dust events in the EM and the exceptional character of this event is emphasized by a comparison with climatological studies (Singer et al., 2003; Alpert et al., 2004; Dayan et al., 2008).

3.2 Course of events

In the following, a detailed analysis of the development stages and responsible atmospheric drivers which lead to the severe dust event is provided. The simulated convection and its interaction with dust emission is investigated in depth. Unfortunately, the region where the MCS and the first stages of the CPOs occur are located in the Syria-Iraq border region, which is not covered by a meteorological observation network. Therefore, no surface observations are available and the event can only be analysed using satellite data, which nevertheless yields interesting results. Figure 4 provides a schematic depiction of the event stages as well as their horizontal extent and course which are referred to in the following.

First cold-pool outflow, heat low and Eastern Mediterranean sea-breeze

During the night from 05 to 06 September 2015 a convective system exists over the Turkey-Syria border region. It is fuelled by the inflow along the eastern side of the RST. The system moves towards the north-east along with the mean flow direction above 500 hPa. Due to the favourable position of the convective system in front of the mid-tropospheric through axis, it

Atmos. Chem. Phys. Discuss., doi:10.5194/acp-2017-11, 2017
Manuscript under review for journal Atmos. Chem. Phys.
Published: 3 February 2017

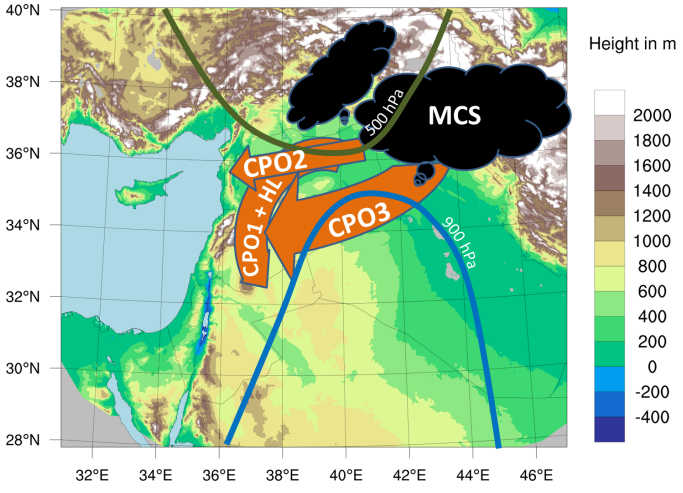

Figure 4. Schematic depiction the main dust event stages and atmospheric features. Colour-coded is the topography as used by the finest domain. Coloured lines represent average geopotential height of pressure levels. Labels refer to the description used in the text. Arrow size corresponds to event magnitude and arrowhead size to event speed.

intensifies during the course of the night. However, in contrast to subsequent systems, it lacks the full meso-scale organization of convection, possibly due to less favourable wind-shear conditions. During the early morning hours of 06 September 2015, the convective system produces a first, weak cold-pool outflow (termed CPO1 in the following) which remains decoupled from the surface due to the stable nocturnal boundary layer. As soon as the sun rises, the downward mixing of momentum increases and dust is picked up (a comparison of ICON-ART modelling results with satellite observations is shown in fig. A1). The high surface wind speeds are intensified and sustained during the day by a strong and shallow heat low (HL) forming in the developing boundary layer. The heat low is located in the tip of the RST and centred above Syria where temperatures during 06 September reach values above 45°C.

During the course of the day, the flow structure created by the CPO1 in combination with the heat low above Syria interacts with the land inward penetrating sea breeze from the Mediterranean Sea, creating strong southward transport of dust towards Jordan. From 10 UTC onwards, the atmospheric instability created by boundary layer heating and upper level cold air advection is released and deep convection starts to develop over the Syria-Iraq border region and Zagros mountain range in the RST inflow region. From SEVIRI Meteosat satellite images a second, convective cold pool outflow (CPO2) which travels west from the Zagros mountain range is detectable at 12 UTC. This CPO2 travels fast towards west in the RST flow structure and supported by the heat low. The reinitialization of ICON-ART with IFS at 12 UTC impairs the CPO2 development due to the termination of convective structures. However, the main flow structures are still captured as the subsequent development shows.

The lifting caused by the gust front of CPO2 triggers initiation of deep convection over the Syria-Iraq border region which organizes into a MCS around 18 UTC. By this time the CPO2 has already travelled far into Syria. The MCS starts to develop a marked, third cold pool outflow (CPO3) from 20 UTC onwards. The CPO3 travels in the wake of CPO2, but in a more southerly

Atmos. Chem. Phys. Discuss., doi:10.5194/acp-2017-11, 2017
Manuscript under review for journal Atmos. Chem. Phys.
Published: 3 February 2017

Atmospheric Chemistry and Physics Discussions

direction. The strong third cold pool flow towards the south counters the inflow from southerly directions along the eastern flank of the RST, thereby lifting the warm and moist air masses. (a comparison of ICON-ART model results and SEVIRI RGB dust product observations as well as CALIPSO backscatter measurements is shown in fig. A2 and fig. A3)

Past midnight on 07 September and explosive intensification of the MCS takes places due to the favourable atmospheric conditions. It develops a sharply defined, curved rainfall pattern in front of which the CPO3 is strongly intensified. In connection with the only slowly advancing upper atmospheric trough, which causes quasi-geostrophic forced ascent, and the orographic support from the Zagros mountain range, the MCS remains quasi-stationary over the next 12 hours. Due to the long duration and separation of the up- and down-draft region the MCS is able to produce an enormous amount of cool, moist air and a mighty CPO3 downstream a line shaped rainfall pattern. During the course of the night, the southerly direction of the CPO3 is deflected into a westerly flow direction by the RST flow structure and its inflowing air masses. The night-time spread of the CPO3 towards west is crucial due to its subsequent interaction with the developing boundary layer mixing during daytime. Dust pick-up in CPO2 and CPO3 is limited during the night but increases as soon as boundary layer mixing increases due to solar insolation. At 10 UTC 07 September all satellite platforms are available and an in-depth analysis is conducted.

3.3 Meso-scale convective system and cold-pool outflows

An in-depth analysis of model results and comparison to satellite observations is conducted at 10 UTC 07 September (fig. 5). The simulated MCS has passed its most intensive development stage approximately four hours earlier. The main MCS features are still visible, although it is in the stage of dissolution due to the shift of the upper atmospheric trough towards east (fig. 5 c)). The convection is organized along the orographic features of the Zagros mountain range, exhibiting a sharp line shaped rainfall distribution. Possibly, the convective structure is also shaped by a weak cyclogenesis taking place further east due to the favourable upper-tropospheric conditions. The cirrus cloud anvil extends far to the north-east as it is transported away by the upper level flow. Downstream the line-shaped rainfall distribution near surface wind speeds increase strongly as the CPO3 reaches the surface (fig. 5 b)). Wind speeds above 12 m s^{-1} are modelled inside the CPO3 region. The southern edge is distinct and counters the inflow from the Persian Gulf region. The edge is also clearly recognizable in the 2m-dew point temperature (2m-DPT) field which is a good indicator for CPOs due to the change in air mass characteristic (Knippertz et al., 2007). The difference in 2m-DPT between the CPO3 and the surrounding air masses is approximately 10°C (fig. 5 d)). Dust has been picked up in large quantities over the previous hours with increasing boundary layer turbulence and dust optical depth (DOD) values above 2 are modelled in the CPO3 region (fig. 5 a)). The maximum DOD value is 4.15, it is reached in an area close to the leading edge of CPO3 which shows the highest values of DOD.

Towards north, the DOD exhibits a sharp gradient (northern boundary of CPO3 dust plume in fig. 5). At closer inspection of the wind and dew point temperature fields it becomes apparent that the decrease in DOD is not linked to the extent of the CPO3 in north-western Syria (fig. 5 b) and d)). This is due to the orography and the soil-type distribution in the region, a change in soil type towards less-emitting light clay and the increase in elevation are responsible for the reduced DOD towards north. The northern edge of the aged CPO2 is marked by a line of convective clouds over the Taurus mountain range, here a second but less distinct gradient in DOD is visible. In the south-western part of Syria, entering Jordan, the remains of CPO2 are also still

Atmos. Chem. Phys. Discuss., doi:10.5194/acp-2017-11, 2017
Manuscript under review for journal Atmos. Chem. Phys.
Published: 3 February 2017

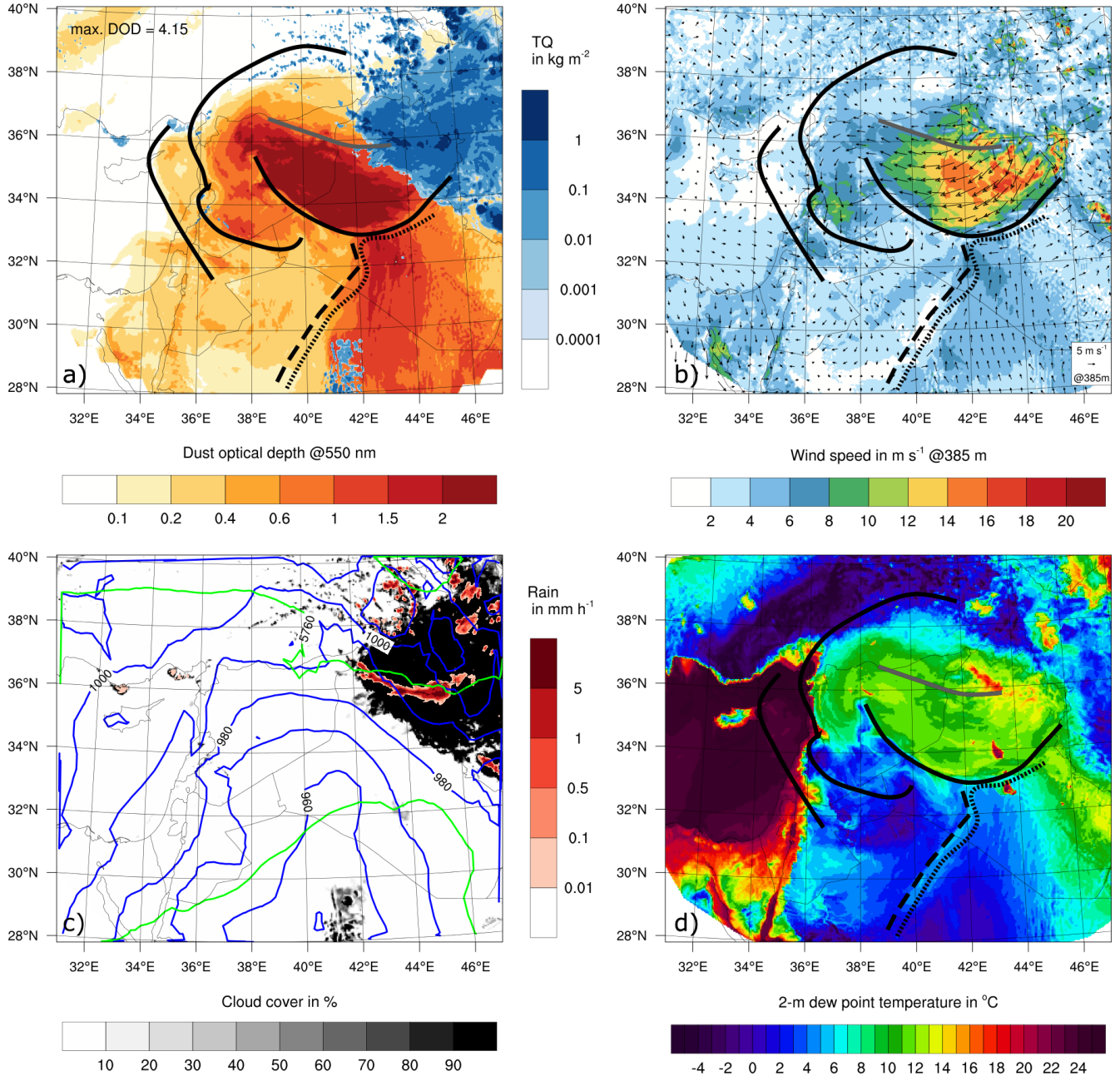

Figure 5. ICON-ART model results at 10 UTC 07 September. Displayed are: a) Dust optical depth at 550 nm overlain with column integrated hydro-meteor content TQ (cloud water, cloud ice and graupel). b) Wind speed at 385 m model height and wind velocity as vectors. c) Fractional cloud cover and surface rain rate colour coded. Blue lines show geopotential height of 900 hPa level at 10 gpm intervals, green lines show geopotential height of 500 hPa level at 20 gpm intervals. d) 2m-dew point temperature. From west to east solid black lines mark leading edges of CPO1, CPO2 and southern CPO3 boundary. Gray line marks northern dust plume boundary inside CPO3. Dashed line marks merged EM Sea-breeze front from 05 and 06 September. Dotted line marks frontal region of inflow.

Atmos. Chem. Phys. Discuss., doi:10.5194/acp-2017-11, 2017
Manuscript under review for journal Atmos. Chem. Phys.
Published: 3 February 2017

Atmospheric Chemistry and Physics Discussions

detectable by an elevated DOD above 1 and higher wind speeds up to 10 m s^{-1}. In addition, at a closer look the formation of small convective clouds above the nose of CPO2 can be seen in the ICON-ART model results. The aged CPO2 re-intensifies and the arc clouds develop further during the course of the day.

Comparing ICON-ART model results to the corresponding satellite observations shows that all modelled features are confirmed by the observations (fig. 6). A comparison of the SEVIRI cloud cover with ICON-ART results shows that the cirrus anvil of the MCS has a greater lateral extension in the model, whereas it is confined around 36°N in the observations (fig. 6 b)). In addition, the MCS has moved further east by approximately 2° in reality. Taking the area with the brightest colour as a proxy for the strongest deep-convective area, the MODIS visible satellite image (fig. 6 c)) shows good agreement with the line of highest integrated hydro-meteor content in ICON-ART (fig. 6 a)).

The structure of the MCS determines the shape of the outflow, therefore differences in outflow structure can be identified as well. Again, the CPO3 is more sharply confined between 34°N and 36°N in the observations, whereas it shows a bow shaped southward extension beyond 34°N in ICON-ART. The northward boundary of CPO3 is modelled accurately, with a northward deviation at the western tip. Modelled DOD is higher in ICON-ART when compared to MODIS AOD in the eastern part of CPO3 and lower in the western part of CPO3 (fig. 6 d)). Unfortunately, no measurements by MODIS are available over sea. For the eastern part of CPO3 the MODIS AOD measurements seem doubtful when comparing to the MODIS visible satellite image (although it is reduced by a value of 0.3 to account for other background aerosols measured by MODIS, the discrepancy is much larger than this).

The aged CPO2 spreading towards the north is detected by all satellite instruments, it is modelled with an offset towards the north-east by ICON-ART (northernmost solid black line in fig. 6). Noticeable are arc clouds forming above the Taurus mountains in simulation and reality. The south-western boundary of the aged CPO2 is modelled correctly in the Golan Heights region. However, towards the west and south the CPO2 has advanced further in reality than in the model, as all measurements show a southern edge of the CPO2 which is just about to cross the border into Saudi-Arabia. Aerosol optical depths retrieved by MODIS are in the range of 1.5 whereas ICON-ART simulates values in the range of 1. In this case, the MODIS measurements seem more realistic when compared to the visible satellite picture. A possible reason for the underestimation of DOD magnitude in the model are reduced dust emissions due to an unrealistic land use characterisation. Due to recent changes in the region (see Sec. 2) an update of the land-use classes can be expected to yield significant improvements of modelled DOD magnitude.

The vertical structure of the dust plume can be investigated at this point in time with the help of a CALIPSO overpass which occurred at 10.35 UTC. Results along the flight track are shown from south to north in figure 7. The southern inflow region towards the MCS shows high values of the extinction coefficient in ICON-ART and attenuated backscatter in CALIOP measurements. The height of the dust plume is between $5-6$ km, with decreasing height towards the MCS. Just south of the main CPO3 dust plume, in a region from $32-33$°N both show a decrease in dust concentrations at upper levels. However, a difference exists in the near surface values up to 2 km, where CALIOP reports high values of total attenuated backscatter but ICON-ART shows a minimum in extinction coefficient. The reason for this difference becomes clear when looking at the CALIPSO ground track again in figure 6. The satellite passes the region where the merged one and two day old sea-breezes from the Mediterranean penetrate the RST inflow in a cyclonic rotational movement. The frontal structure is visible in figure 5

Atmos. Chem. Phys. Discuss., doi:10.5194/acp-2017-11, 2017
Manuscript under review for journal Atmos. Chem. Phys.
Published: 3 February 2017

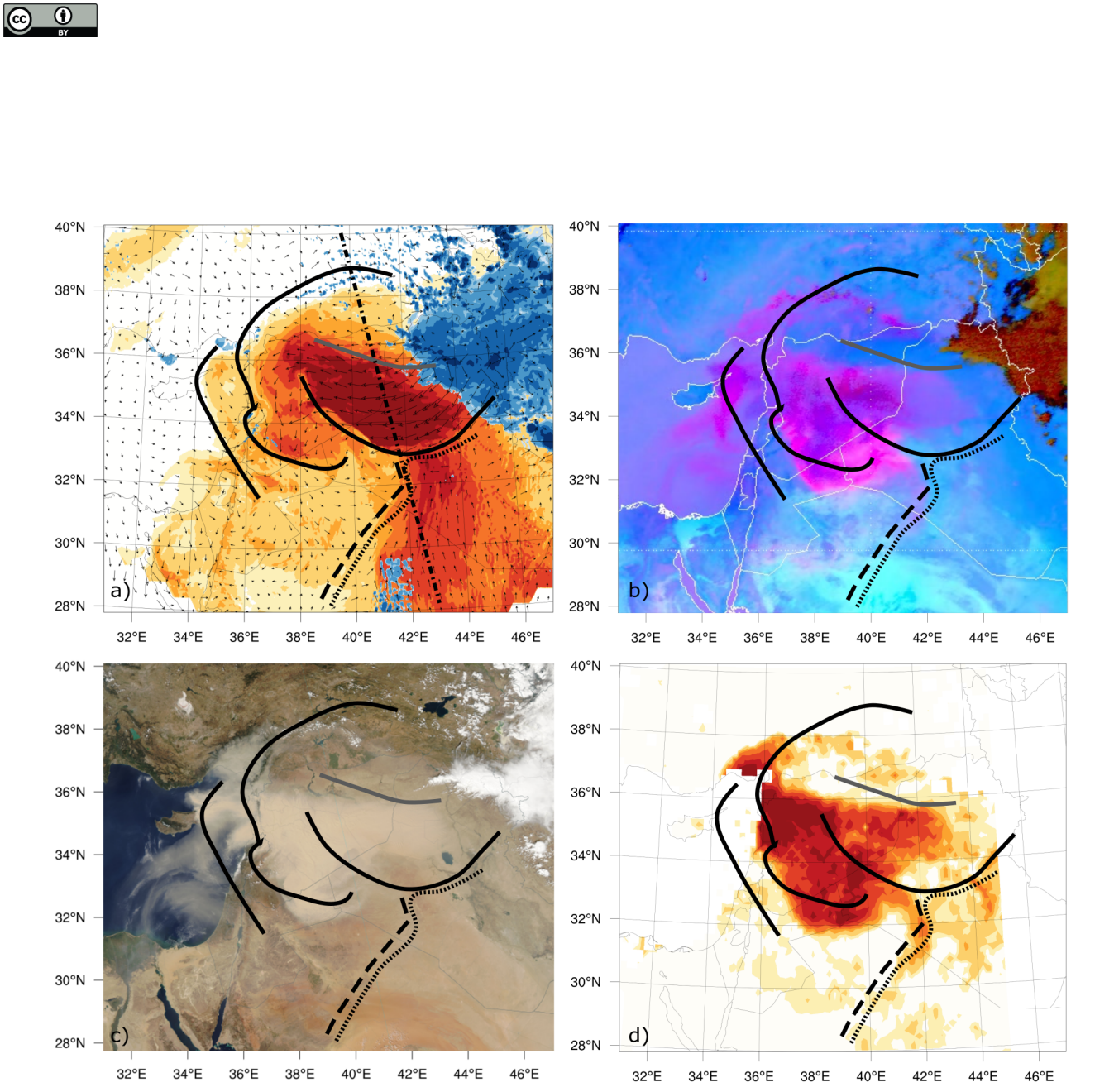

Figure 6. ICON-ART model results and satellite observations for 10 UTC on 07 September. Axis for dust optical depths, column integrated hydro-meteor content and event marks as in figure 5. Displayed are: a) ICON-ART dust optical depth, column integrated hydro-meteor content and wind velocity. b) SEVIRI RGB dust product (Kerkmann et al., 2015). c) Aqua MODIS VIS satellite image, overpass at 10.35 UTC (NASA Worldview, 2016). d) Aqua MODIS aerosol optical depth retrieval using DB2 algorithm (AOD-0.3) (Levy and Hsu, 2015), overpass at 10.35 UTC. Chain dotted black line marks CALIPSO ground track at 10.35 UTC.

Atmos. Chem. Phys. Discuss., doi:10.5194/acp-2017-11, 2017
Manuscript under review for journal Atmos. Chem. Phys.
Published: 3 February 2017

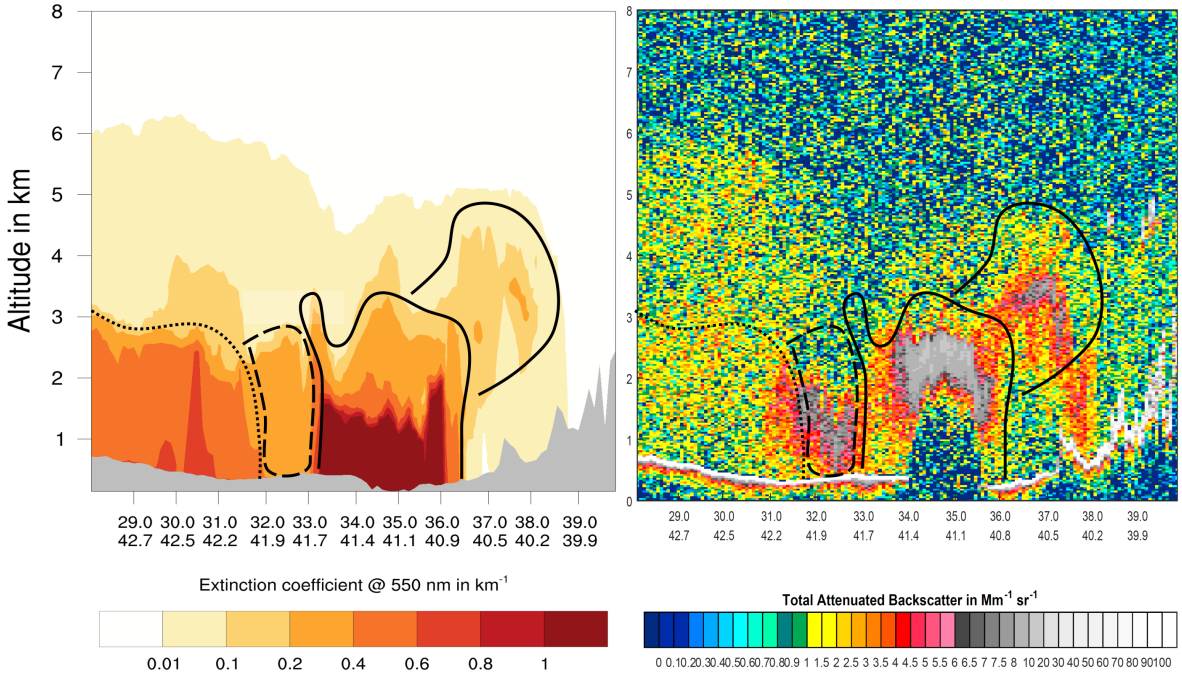

Figure 7. Vertical cross-section of ICON-ART model results for 10 UTC on 07 September and CALIPSO satellite observations from south to north along ground track in figure 6. Left side: ICON-ART mineral dust extinction coefficient. Right side: Total attenuated backscatter as measured by CALIOP. No quantitative comparison is possible as two different measures are displayed. Southern dotted black line marks inflow region. Dashed black line marks aged EM Sea-breeze penetrations region. Southern solid black line marks CPO3. Northern solid black line marks aged and lifted CPO2.

as a thin line in 2m-DPT, a gradient in DOD and a change in wind velocity along the front (as can be expected from a frontal structure). ICON-ART is able to simulate the re-intensifying sea-breezes, thereby enabling the above analysis, however no dust pick-up is connected with the frontal structure. This is due to the less emissive soil type in the region passed by the front. In reality, however, dust was picked up by this frontal structure, this is detectable in all three satellite measurements (fig. 6). As a result, CALIOP reports high values of attenuated backscatter in this region whereas ICON-ART simulates a minimum due to the clean air characteristics of the sea breeze.

The main CPO3 dust plume is distinct in both figures with ICON-ART simulating an elevated nose of the CPO3. The above discussed differences in CPO3 structure are identifiable again. ICON-ART simulates a wider and more shallow outflow whereas in reality it was more confined. In addition, the observations show an approximately one kilometre higher main dust plume compared to ICON-ART. Altitudes below 2 km are marked as no signal regions in the CALIPSO feature mask due to the attenuation of the lidar signal (not shown). On the northern side of the plume beyond 36°N a minimum captured by both is visible, once more illustrating the well simulated northern boundary of the CPO3 in this region. Further towards the north the

Atmos. Chem. Phys. Discuss., doi:10.5194/acp-2017-11, 2017
Manuscript under review for journal Atmos. Chem. Phys.
Published: 3 February 2017

Atmospheric Chemistry and Physics Discussions

overarching dust plume structure consisting of dust picked up by the aged CPO2 is represented very similarly in simulation and measurement.

Summarizing, a northward deviation of the flow structure in ICON-ART can be identified both for CPO2 and CPO3 although the overall intensity and characteristics are simulated well. The combination of the northern deviation towards less dust emitting soil types and the wider, less well defined main outflow region reduce the amount of DOD over western Syria due to a less intense channelling of the CPO3. Furthermore, the re-intensification of the aged CPO2 is modelled by ICON-ART, however, it was observed with greater magnitude in reality. The reduced amount of dust in the atmosphere in ICON-ART leads to a reduction in long range transport of dust towards the EM over night.

3.4 Long-range transport to the Eastern Mediterranean

From 10 UTC onwards on 07 September, the MCS starts to dissipate and is in the course advected east along with the mean flow conditions above 500 hPa. The CPO3 airmass created during the night spreads south-west during daytime on 07 September. At all times it shows the characteristic features associated with CPOs such as an increase in surface wind speed, higher dew point temperatures and an arc cloud forming above the leading edge during the afternoon hours. The high surface wind speeds and turbulent mixing inside the CPO3s result in enormous dust emissions during daytime, consequently the dust is transported within the full boundary layer height up to 5 km.

With nightfall on 07 September the CPO2 and CPO3 merge. As the merged CPO is still located in the western, downstream flank of the RST the air mass and dust contained within it are advected fast towards south-west over the course of the night. The Dead Sea Rift Valley is passed by the dust mass after midnight on 08 September, with the dust plume interacting with the complex orography. A comparison of simulated dust optical depth with satellite observations for 11 UTC 08 September shows that ICON-ART values are one order of magnitude higher than other simulation results in the northern part of the EM (see Sec. 1 and fig. A4). However, dust transport across the Dead Sea Rift Valley into the southern EM is not simulated with the correct magnitude by ICON-ART despite the overall dust plume structure being captured well. Therefore, the transport into this region is analysed further in section 3.4.1. Overall, a significant dust forecast improvement is achieved through convection permitting simulations with ICON-ART at 47 hour forecast time without data assimilation. During daytime on 08 September the dust plume is mostly stationary in the EM and influenced by the local circulation systems. In visible satellite pictures, the dust can be seen to remain in the EM at high concentrations over the course of the next four days. This period is not investigated as a part of this study as the scope of this work is the analysis of the generating mechanisms.

Due to the problems in simulating dust transport towards the southern EM with the correct magnitude, the next section investigates the timing and structure of the CPO arrival in Israel in reality and simulation. This reveals the interaction of the dust plume with the orography in the region in the form of super-critical flow conditions and connected, subsequent hydraulic jumps.

Atmos. Chem. Phys. Discuss., doi:10.5194/acp-2017-11, 2017
Manuscript under review for journal Atmos. Chem. Phys.
Published: 3 February 2017

Atmospheric Chemistry and Physics Discussions

3.4.1 Environmental station data

In this section the simulated dust concentrations are compared to measurements from three stations in Israel. The selected stations are Afula, Jerusalem (Bar Ilan) and Ashdod (Nir Galim) as they all show individual dust concentration characteristics during the event (see fig. 9 c) for a map of the station locations).

The modelled dust plume reaches Afula first, this is also where the highest values of DOD up to 1.5 are achieved because of the previously discussed transport through the Golan Heights (first row in fig. 8). A few hours later, Jerusalem shows an increase and its peak optical depth. DOD increases even later in Ashdod due to its location in the south-west, but the DOD values reach higher levels than in Jerusalem due to the lower altitude of the station.

The large difference in absolute values of modelled and measured PM10 concentrations (second and third row in fig. 8) is caused by the inadequately modelled interaction of the dust plume with the complex orography of the Dead Sea Rift Valley as the next section shows.

Despite the large difference in absolute values, the dust transport processes can be studied by comparing the course of the measured and modelled PM10 concentrations. Although the DOD in Afula reaches highest values during the night already, peak concentrations at 57 m surface elevation are only measured after noon on 08 September. This is due to arrival of the dust plume in 1 km height. Consequently, the onset of turbulent mixing is needed to transport the high dust concentrations towards the surface. The discussed processes are modelled sufficiently by ICON-ART, as it shows a very similar shape of the PM10 concentrations curve compared to the measurements with a peak at 12 UTC.

Highest overall PM10 concentrations are measured by the Jerusalem station. It shows the earliest and most pronounced peak of all stations at 08 UTC. This is also the case in ICON-ART, although with a shorter peak duration. The earlier and higher peak concentrations in Jerusalem are to due to the elevated location of the measurement station at 770 m which is almost inside the dust plume. For this reason, PM10 concentrations are also more correlated with the shape of the DOD curve at this station. A secondary peak after sunset is visible in the measurements and model results. This peak can be explained by the formation of a stable nocturnal boundary layer, in which the dust from higher altitudes settles to the ground.

The station in Ashdod measures the lowest PM10 concentrations at nearly all times, despite showing the highest values of modelled DOD past noon. This is due to the early onset of the Mediterranean Sea breeze at the shore which brings in cleaner air compared to the other stations. The reason for the cleaner nature is the less turbulent character of the marine boundary layer compared to the boundary layer over land. Consequently, it mixes less dust to the surface, a feature which is captured well by ICON-ART.

ICON-ART fails to reproduce the measured low values of global radiation because for the radiative impact the absolute values of the dust concentration are of importance. The differences visible in the DOD above the stations manifest themselves in differences between the modelled amount of global radiation at the stations.

Atmos. Chem. Phys. Discuss., doi:10.5194/acp-2017-11, 2017
Manuscript under review for journal Atmos. Chem. Phys.
Published: 3 February 2017

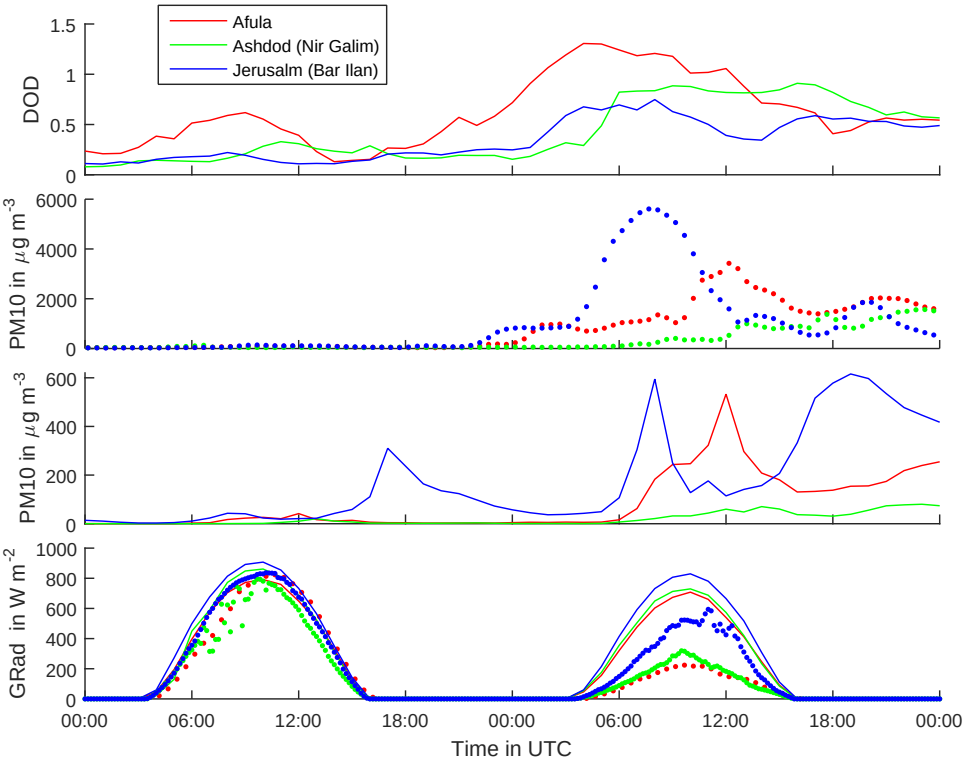

Figure 8. Observations and model results for three stations in Israel for 07 and 08 September. Points denote observations and solid lines model results. Please note the difference in y-axis scaling by a factor of ten between the second and third sub-plot. Shown are from top to bottom: 1. Modelled dust optical depth 2. Measured PM10 concentrations. 3. Modelled PM10 concentrations. 4. Global radiation (GRad), the values shown are for Afula, Bet Dagan and Jerusalem (Givat Ram) due to data availability.

3.4.2 Hydraulic jump upstream the Dead Sea Rift Valley

In order to understand the failure of the model to forecast dust in Israel with the correct magnitude the transport processes upstream have to be investigated in more detail.

In figure 10 a cross-section of ICON-ART results along a cross-section through the Golan heights is displayed for 03 UTC 08 September. The location of the cross-section and according meteorological situation is illustrated in figure 9. The arrival of the dust plume is simulated above a height of 1 km in Israel. This is in good agreement with measurements of the dust plume height in Israel which also report an arrival of the dust plume in 1 km height (Alpert et al., 2016).

Remarkable is a wave structure in the extinction coefficient on the lee side of the Golan Heights (fig. 10). In the region of the wave structure, after passing the Golan Heights crest, the vertical depth of the dust plume decreases significantly to a few hundred meters. The plume expands and returns to its original height again in an abrupt expansion further to the west which

Atmos. Chem. Phys. Discuss., doi:10.5194/acp-2017-11, 2017
Manuscript under review for journal Atmos. Chem. Phys.
Published: 3 February 2017

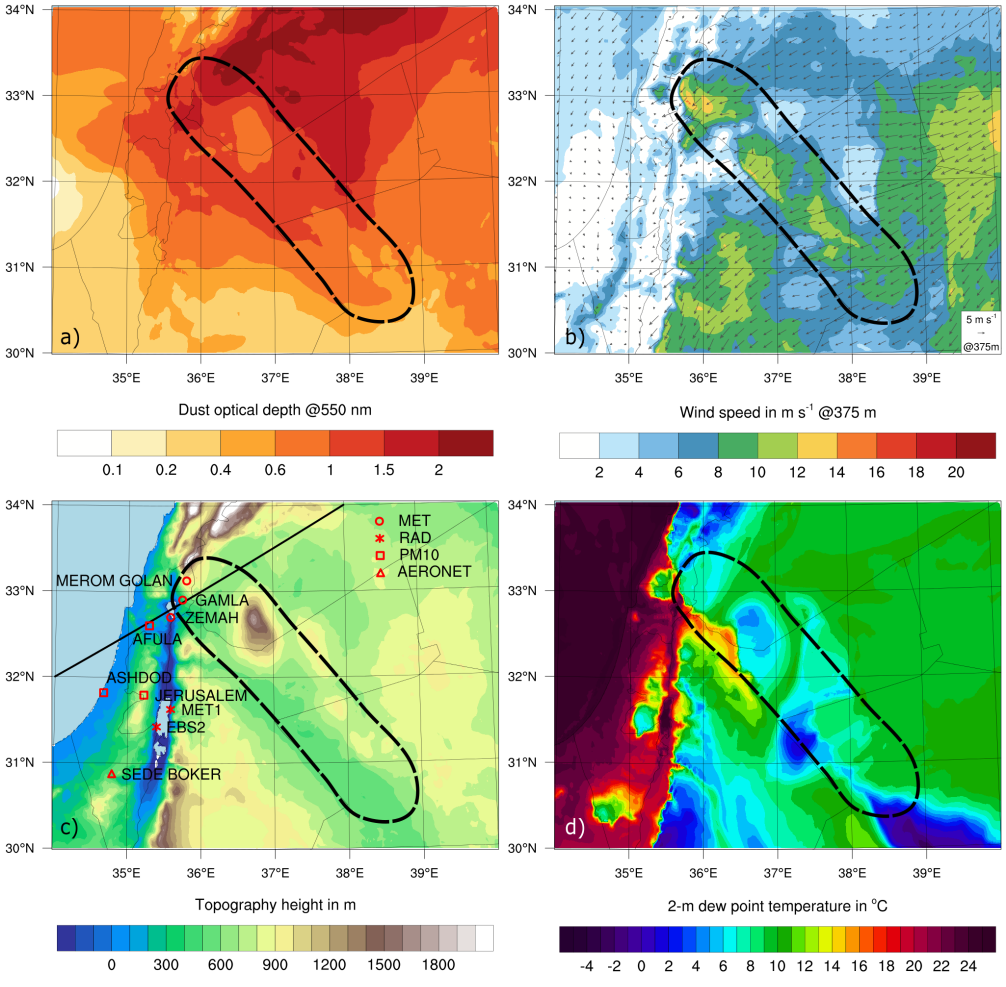

Figure 9. ICON-ART model results at 03 UTC 08 September, same as figure 5 but for the Dead Sea Rift Valley area. The bottom left plot shows the orography in the region colour-coded. The dashed black line marks the region where super-critical flow conditions and the subsequent hydraulic jump occur. The solid black line in c) shows location of ICON-ART vertical transect displayed in figure 10. In addition, location and names of stations used for comparison of results are displayed.

Atmos. Chem. Phys. Discuss., doi:10.5194/acp-2017-11, 2017
Manuscript under review for journal Atmos. Chem. Phys.
Published: 3 February 2017

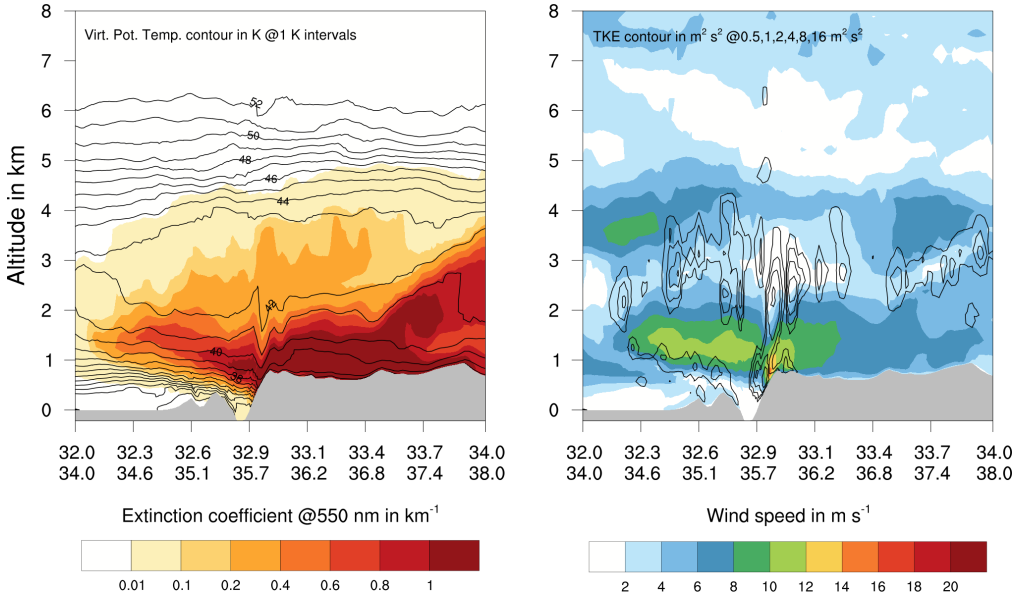

Figure 10. ICON-ART model results along a vertical cross-section from 32°N, 34°E to 34°N, 38°E at 03 UTC 08 September. Displayed on the left side is the colour-coded extinction coefficient overlain with virtual potential temperature contours. On the right side wind-speed is colour coded and overlain with turbulent kinetic energy contours.

is accompanied by a sharp decrease in flow speed. The reason for this behaviour is the existence of a flow phenomena termed 'hydraulic jump'.

Hydraulic jumps are connected to flows going from a sub-critical flow stage with Froude numbers Fr smaller one, to a super-critical flow stage, with Froude numbers greater one. According to Drobinski et al. (2001) the Froude number can be calculated as:

$$Fr = \frac{U}{\sqrt{gh}} \cdot \sqrt{\frac{\Theta_v}{\Delta\Theta_v}}. \quad (1)$$

Thereby, U denotes the wind speed and Θ_v the virtual potential temperature in the atmospheric boundary layer, chosen at a representative level and $\Delta\Theta_v$ the temperature inversion at the boundary layer top. Further, g is the gravitational acceleration and h the atmospheric boundary layer height.

Hydraulic jumps have been documented penetrating the Dead Sea Valley for flow conditions from the west (Metzger, 2016). The flow across the Golan Heights shows characteristic features of a super-critical flow with a subsequent hydraulic jump (see figure 10). These are:

1. A continuous decrease in mixing layer height detectable in the virtual potential temperature and extinction coefficient fields leading to a compressions of the sub-critical flow from east to west.

2. A sharp decrease in the vertical flow depth, connected to a rise in flow speed, after passing the orographic Golan Heights crest. This denotes the transformation of the flow state from sub- to super-critical.

Atmos. Chem. Phys. Discuss., doi:10.5194/acp-2017-11, 2017
Manuscript under review for journal Atmos. Chem. Phys.
Published: 3 February 2017

Atmospheric Chemistry and Physics Discussions

3. A subsequent sudden increase in flow depth when the flow state reverts to the sub-critical stage again inside the Dead Sea Rift Valley. This is accompanied by a sharp decrease in flow speed and connected to an increase in atmospheric turbulence.

An approximate calculation of the Froude number upstream and downstream the Golan Heights crest height with average flow conditions as simulated by ICON-ART confirms the conversion of the flow state:

$$Fr_{upstream} = \frac{8\ \mathrm{m\ s^{-1}}}{\sqrt{9.8\ \mathrm{m\ s^{-2}} \cdot 1200\ \mathrm{m}}} \cdot \sqrt{\frac{312\ \mathrm{K}}{2\ \mathrm{K}}} = 0.9,$$

$$Fr_{downstream} = \frac{12\ \mathrm{m\ s^{-1}}}{\sqrt{9.8\ \mathrm{m\ s^{-2}} \cdot 800\ \mathrm{m}}} \cdot \sqrt{\frac{313\ \mathrm{K}}{2\ \mathrm{K}}} = 1.7.$$

Hydraulic jumps have been investigated and suggested as dust generating mechanisms (Cuesta et al., 2009). Their existence and interaction with the orography under strong easterly flow conditions has been proven for the Sahara (Drobinski et al., 2009). As the gust front of CPO3 reaches the Dead Sea Rift Valley almost along its full length, the flow reaches supercritical stage in the vicinity of many prominent orographic features (fig. 9 b)). Consequently, the widespread existence of hydraulic jumps in connection with the upstream super-critical flow is assumed to be responsible for dust emissions on the eastern side of the Dead Sea Rift Valley. Dust emission in the region is assisted by the timing of the event, as in September the soil in the region is most erodible due to the preceding hot and dry summer.

The existence of hydraulic jumps is modelled by ICON-ART and detectable along many cross-sections and at different times in the region. Some of them occur on the lee-side of much less pronounced orographic features such as the mountain structure visible at 33.5°N, 37.0°E in figure 10. Although ICON-ART simulates the flow phenomena, the location and magnitude of the hydraulic jumps need to be validated in order to evaluate the simulation quality.

3.4.3 Meteorological station measurements

The validation is done with the help of three meteorological stations approximately along the model cross-section through the Golan Heights. The locations and names of the stations used are marked in figure 9 c). Unfortunately, no measurements are available in Jordan, where the existence of the hydraulic jumps is detectable in many places in ICON-ART and where the more erodible state of the soil is assumed to be responsible for high dust emissions.

The measurements of three meteorological stations are displayed together with the respective model results for their location in figure 11. The arrival of the main dust plume is simulated by ICON-ART past 18 UTC on 07 September. Subsequently, DOD values above 1.5 are reached during the night.

The development of the super-critical flow regime penetrating the Dead Sea Rift Valley is observed at two meteorological stations. It is detectable by marked, high wind speeds, a change in wind direction towards east and a sudden increase in temperature by approximately 4°C. The higher Merom Golan station is first affected shortly before 18 UTC, whereas the lower Gamla station experiences high wind speeds only from 20 UTC onwards. Interestingly, confirming the super-critical flow theory, the highest values of wind speed are measured in Gamla around midnight. This is because the flow has more potential for gravitational acceleration down to 405 m compared to 950 m. Zemah, the station at the floor of the Dead Sea Rift Valley at

Atmos. Chem. Phys. Discuss., doi:10.5194/acp-2017-11, 2017
Manuscript under review for journal Atmos. Chem. Phys.
Published: 3 February 2017

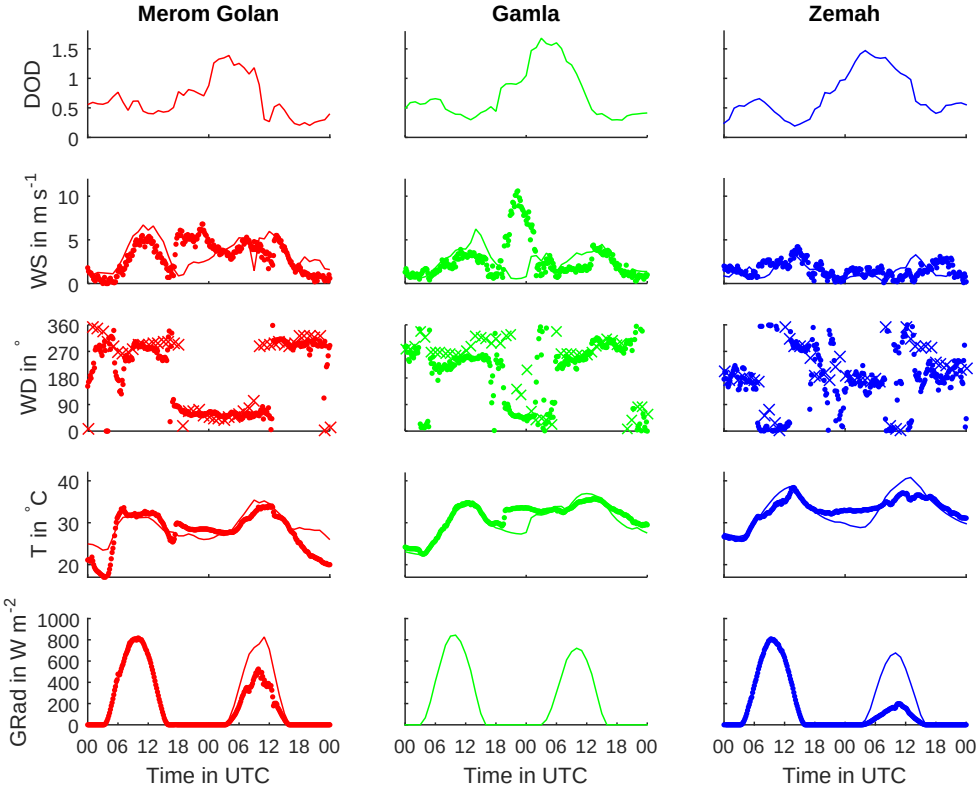

Figure 11. Observations and model results for three stations in the Golan Heights for 07 and 08 September. Points denote observations and solid lines/crosses model results. Shown are from top to bottom: 1. Modelled dust optical depth 2. Wind speed (WS). 3. Wind direction (WD). 4. 2m-surface temperature. 5. Global radiation (GRad).

−200 m does neither report high wind speeds nor a change in wind direction at any point during the night as the super-critical flow does not reach the valley bottom.

The magnitude and timing of the super-critical flow regime is not captured correctly by ICON-ART, as a comparison of observations with model results shows. Although model results for Merom Golan show an increase in wind speed and a change in wind direction the results are far from the observed intensity and 2 hours late. For the lower Gamla station ICON-ART simulates the arrival of the super-critical flow with a delay of six hours and only a third of the observed intensity. As in the observations, the arrival is detectable in changes of wind speed, direction and surface temperature. The Zemah station and valley floor remains unaffected in ICON-ART as in reality. The possible reasons for the deviation of the simulation from reality include an unrealistic night-time boundary layer regime, incorrect atmospheric conditions upstream of the valley and a delayed arrival of the CPO3. As a result, possible mineral dust emissions due to the super-critical flow cannot be captured by ICON-ART. Through its destabilizing night-time boundary layer effect mineral dust itself can provide a positive feedback

Atmos. Chem. Phys. Discuss., doi:10.5194/acp-2017-11, 2017
Manuscript under review for journal Atmos. Chem. Phys.
Published: 3 February 2017

Atmospheric Chemistry and Physics Discussions

mechanism to higher near surface wind speeds and again higher dust emissions in the super-critical flow region. This is visible in the Zemah measurements, where the observations show much higher night-time surface temperature values than the model. This is due to the reduced amount of dust in ICON-ART compared to reality, which thereby underestimates the mineral dust radiative effect.

As a result of the underestimated dust concentrations, ICON-ART is unable to capture the correct magnitude of reduction in global radiation due to mineral dust during daytime. The between day reductions in maximum global radiation for Zemah are modelled to be 125 W m^{-2}, whereas in reality 611 W m^{-2} were observed.

Summarizing, the existence of super-critical flow conditions in the region with connected hydraulic jumps is assumed to cause widespread and strong dust emissions on the eastern side of the Dead Sea Rift Valley. This explains the exceptional amount of dust in the southern part of the EM on 08 September. ICON-ART captures the special flow phenomena, albeit not with the correct magnitude and timing. The lack of a sufficiently developed super-critical flow and resulting high near-surface wind speeds prevents dust emission in Jordan and Israel in the model. Consequently, dust transport into the southern EM is underestimated by an order of magnitude. Nevertheless, ICON-ART provides us with a detailed understanding of previously unknown processes contributing to the historic dust event which makes these findings worthwhile to report.

3.5 Mineral dust radiative effect

The validation of the mineral dust distribution and transport characteristics with satellite and station measurements show overall good agreement between ICON-ART and the observations, especially during the early stages of the event. The simulation therefore allows for investigation of the mineral dust radiative effect. Using ICON-ART, the radiative effect of mineral dust can be studied in detail through the differences between the simulation including mineral dust radiation interaction (ARI) and without it (CTRL). An analysis of the mineral dust radiative effect on surface conditions is conducted at two characteristic points in time during the dust storm development.

The first analysis is performed at 03 UTC 07 September as it shows interesting night-time features due to mineral dust (fig. 12). The point in time chosen is just before sunrise in the region. The mineral dust affected areas show the expected behaviour in terms of its influence on radiative transfer. Net global radiation at night is increased by values between $5 - 50$ W m^{-2}, with higher values in regions with higher aerosol optical thickness (fig. 12 d)). The increase is caused by an increase in down-welling long-wave atmospheric radiation (not shown). Consequently, the amount of energy radiated into space is reduced, which causes a night-time warming of the surface. The reductions in net global radiation towards the east are caused by the daytime effect of mineral dust, as the sun is rising in this region already. The 2m-temperature field outside the CPO3 and MCS region (which themselves are discussed further below) shows the expected behaviour for mineral dust at night with an increase in surface temperature for ARI (fig. 12 c)). Also visible are smaller scale irregularities showing local temperature differences located outside the region affected by mineral dust. These are introduced due to the slightly different location and timing of convection in both runs. The magnitude of the temperature response to mineral dust radiative forcing is large when compared to other studies with values up to 5 K (Tegen et al., 2006; Highwood and Ryder, 2014; Rémy et al., 2015). A possible explanation are the high values used for the imaginary part of the mineral dust refractive index in the near infra-red spectral region, making the

Atmos. Chem. Phys. Discuss., doi:10.5194/acp-2017-11, 2017
Manuscript under review for journal Atmos. Chem. Phys.
Published: 3 February 2017

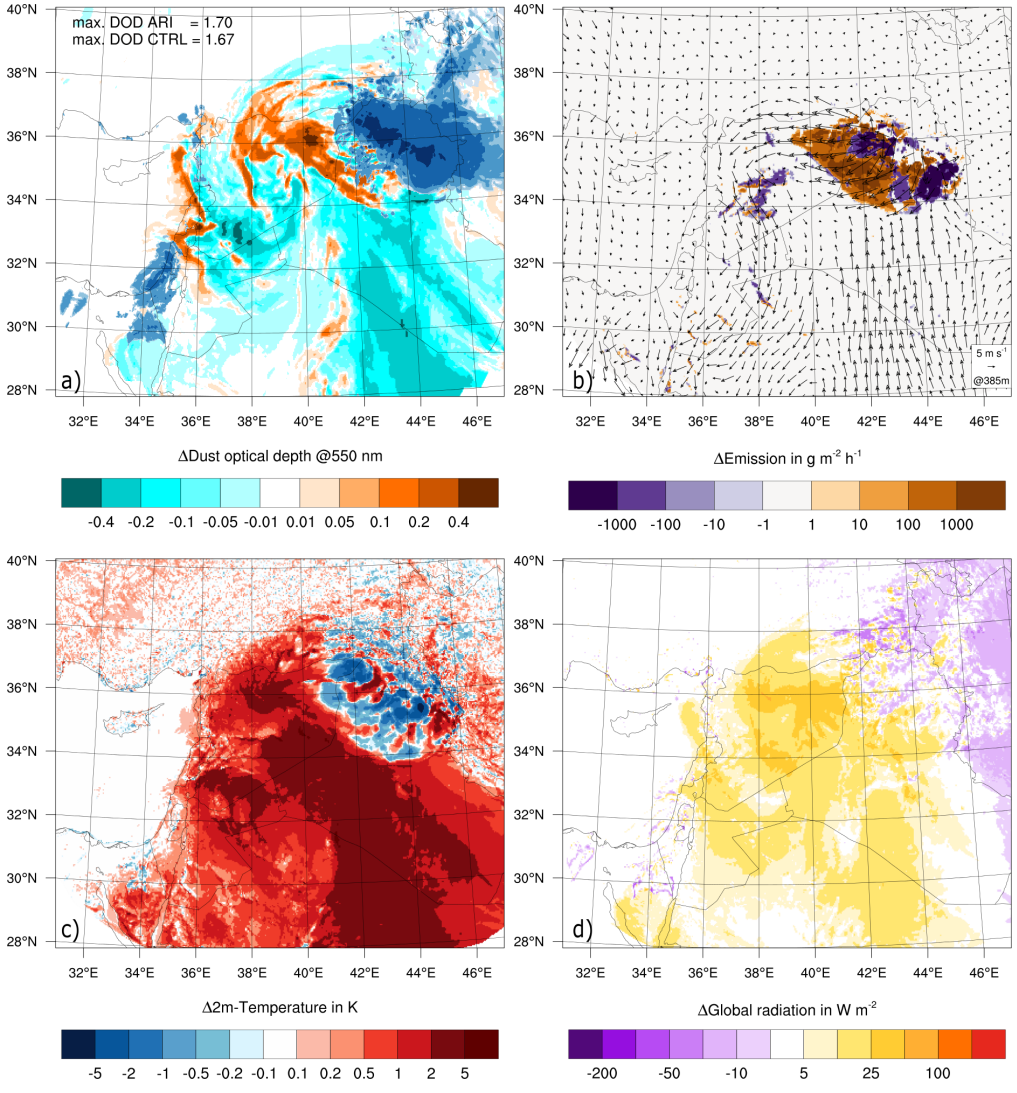

Figure 12. ICON-ART model results at 03 UTC 07 September, all results show ARI-CTRL. Displayed are: a) Column integrated hydrometeor content as in fig. 5 and difference in dust optical depth. b) Wind velocity and difference in hourly mineral dust emission. c) Difference in 2m-temperature. d) Difference in net global radiation at the surface.

Atmos. Chem. Phys. Discuss., doi:10.5194/acp-2017-11, 2017
Manuscript under review for journal Atmos. Chem. Phys.
Published: 3 February 2017

Atmospheric Chemistry and Physics Discussions

dust more absorptive. No homogeneously increased emissions are observed despite the decreased vertical stability outside the CPO3 area (fig. 12 b)). The DOD is lower by more than 0.1 for most regions in the ARI run, although the maxima between runs are similar. This results from the decreased emission during the previous day with a more stable boundary layer during daytime (not shown).

The DOD difference shows regions with an increased DOD at the leading edges of the CPOs in ARI (fig. 12 a)). As the overall maxima of DOD are of comparable magnitude between ARI and CTRL, this can be attributed to a different propagation speed of the CPOs between runs. The CPOs in the ARI run show a higher propagation speed, which is not only detectable in the DOD but also wind speed and 2m-DPT signal, especially at later stages (not shown). In ARI, the CPO with its steep DOD gradient arrives earlier compared to CTRL, therefore a higher DOD is shown for in the leading edge region at the same point in time. Furthermore, the leading edge is more sharply defined in the ARI simulation in general (not shown). The difference in DOD goes hand in hand with differences in dust emission which are also apparent in figure 12.

Inside the CPO3 region a 2m-temperature cooling of more than 2 K can be observed for ARI (fig. 12 c)). This is the opposite of the expected mineral dust night-time effect as discussed above. However, the mineral dust radiative forcing in this region remains positive (fig. 12 d)). Dust emission increases in the ARI run despite a cooler surface, which again is not expected. All findings point towards a more intense CPO3 in the ARI run, which can explain all of the above observations.

A more intense and faster spreading CPO can have multiple reasons:

1. More intense convection leading to more rainfall which can evaporate, this in turn cooling the CPO more. The intensity of the convection can be increased due to a warmer inflowing airmass because of the mineral dust radiative surface heating at night.

2. More potential for evaporation due to a warmer surface boundary layer, also creating a cooler CPO.

3. A more stable stratified and thereby less turbulent CPO, preventing the loss of energy due to turbulent friction.

4. Travel of the CPO into a less stable night-time boundary layer due to mineral dust radiative surface heating. Therefore, less potential and kinetic energy of the CPO needs to be invested in order to lift the stable night-time boundary layer in front. Due to the reduced resistance propagation speed can increase.

The second analysis investigates the day-time radiative effect of mineral dust and is done for 10 UTC on 07 September (fig. 13), this development stage is also analysed in section 3.3. The dominant effect is the reduction in incoming shortwave solar radiation, while the increase in down-welling atmospheric long-wave radiation is of lesser magnitude (not shown). Resulting reductions in net global radiation are more than 200 W m^{-2} in the CPO3 region. The average value at the core of CPO3 in the region bordered by the $34°, 36°$N circles of latitude and $40°, 42°$E meridians is -281 W m^{-2} (fig. 13 d)). The reduction in incoming energy leads to a widespread reduction in 2m-temperature of more than 2 K. The average value in the aforementioned area is -1.4 K. The reduction in surface temperature is less than documented by other studies (Tegen et al., 2006; Helmert et al., 2007; Heinold et al., 2008). Possible explanations are the less absorptive character of mineral dust in ICON-ART with low values of the imaginary part of the refractive index in the short-wave region. Consequently, the dust mostly

Atmos. Chem. Phys. Discuss., doi:10.5194/acp-2017-11, 2017
Manuscript under review for journal Atmos. Chem. Phys.
Published: 3 February 2017

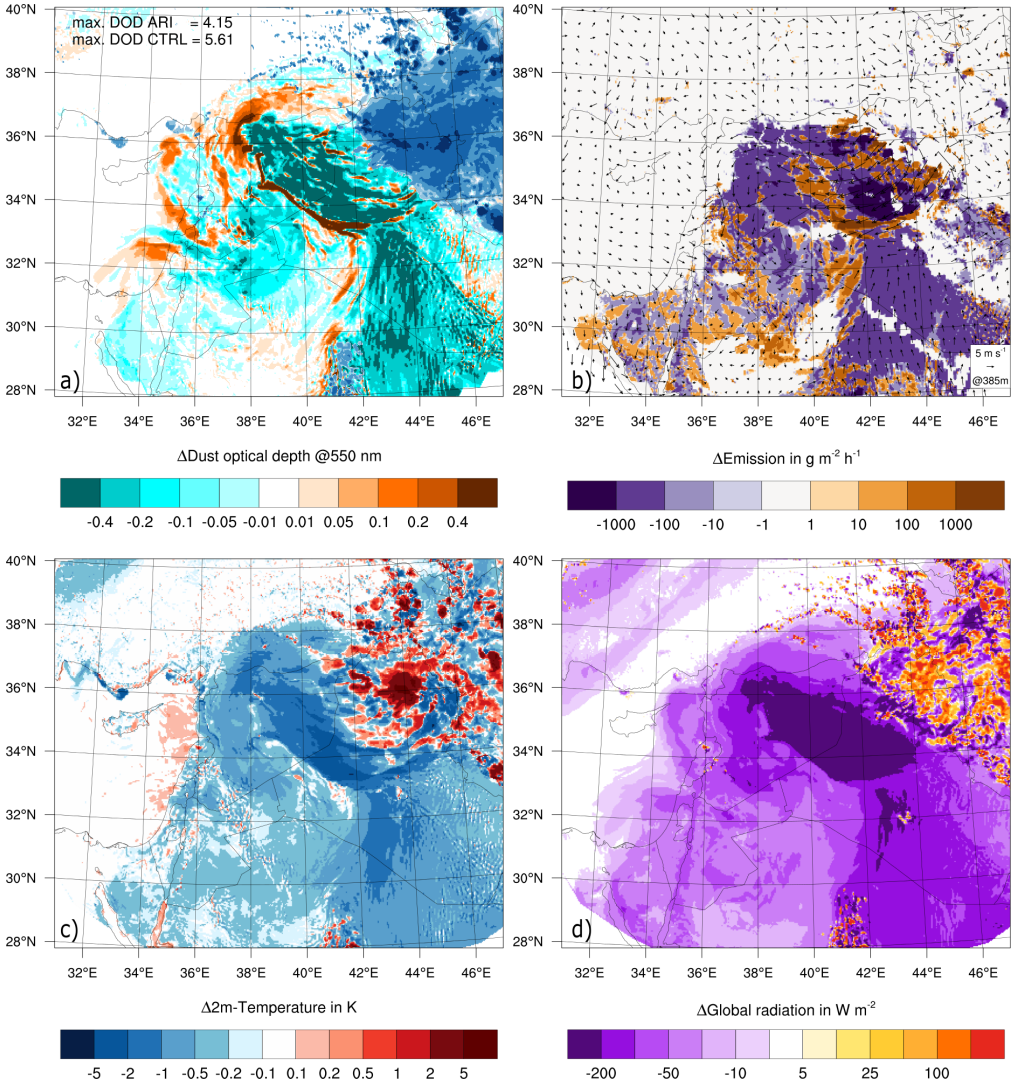

Figure 13. ICON-ART model results at 10 UTC 07 September, same as figure 12.

Atmos. Chem. Phys. Discuss., doi:10.5194/acp-2017-11, 2017
Manuscript under review for journal Atmos. Chem. Phys.
Published: 3 February 2017

Atmospheric Chemistry and Physics Discussions

scatters radiation compared to absorbing it, thereby converting direct radiation to diffuse radiation. As the energy reaches the surface nevertheless, reductions in surface temperature due to mineral dust are smaller than those found by to other studies. A detailed analysis for the 10 UTC situation supports this hypothesis. Decreases in direct shortwave radiation are on the order of 600 W m^{-2} inside the CPO3 region. However, these are countered by increases in diffuse shortwave above 200 W m^{-2}, giving a net reduction in short-wave radiation of approximately 400 W m^{-2} (not shown). Furthermore, the high amount of water vapour contained in the CPOs possibly absorbs and scatters large quantities of solar radiation without dust already, thereby reducing the effect due to mineral dust. An observation which supports this hypothesis is that the reduction in 2m-temperature does not scale linearly with the difference in DOD between inflow and outflow region of the MCS.

The reductions in surface temperature have a stabilizing effect on the boundary layer (Heinold et al., 2008). As a result of the increased boundary layer stable stratification dust emissions decrease almost homogeneously throughout the dust affected region (fig. 13 b)). In addition, this results in a reduced maximum DOD of 4.15 in ARI compared to 5.61 in CTRL for the whole domain. During the late afternoon with maximum boundary layer development this difference increases. At 15 UTC ARI and CTRL show maximum DODs of 6.11 compared to 9.26, respectively. Another marked feature visible in figure 13 is the previously discussed difference in DOD at the CPO leading edges (fig. 13 a)). As the feature is visible over more than 20 hours and in connection with all CPOs this confirms the observation of faster spreading CPOs in simulations including the mineral dust radiative feedback as proposed earlier. The streaks detectable inside the CPO3, where ARI shows higher values of DOD, can be attributed to shallow boundary layer convection which develops earlier and more intensely in the CPO3 region in CTRL due to the lacking vertical stabilization (not shown). Consequently, due to the redistribution of dust by convection the DOD field is more inhomogeneous in the CTRL run (not shown).

4 Conclusions

To our knowledge, this study presents the first sucessful simulation of the September 2015 severe dust event at convection permitting resolution. An active Red Sea Trough situation and the related MCS and CPOs are shown to be responsible for the severe dust event in the Eastern Mediterranean. In addition, the interaction with an intense heat low, the land inward penetrating Eastern Mediterranean sea-breeze and the widespread occurrence of super-critical flow conditions and subsequent hydraulic jumps are suggested as important drivers for dust emission. The mineral dust radiation interaction has been implemented as a new module in ICON-ART. Based on Mie scattering calculations, which are conducted off-line to calculate the mineral dust optical properties, the radiative transfer parameters used by ICON are calculated on-line in ART to account for the mineral dust radiative effect. A new, size dependent parametrization of the mineral dust optical properties is proposed. Furthermore, to our knowledge this is the first study to investigate the mineral dust radiative effect on CPO structure.

Is the forecast of the dust event improved by running convection permitting simulations?

The convection permitting simulation of the dust event with ICON-ART improves the forecast quality decisively. The driving meteorological systems and resulting dust emissions are captured in their horizontal, vertical and temporal structure as is shown

Atmos. Chem. Phys. Discuss., doi:10.5194/acp-2017-11, 2017
Manuscript under review for journal Atmos. Chem. Phys.
Published: 3 February 2017

Atmospheric Chemistry and Physics Discussions

by a comparison with satellite observations. The simulated DOD over Syria and Iraq is of realistic magnitude with values above 2 throughout the main dust event region and maximum values above 6. The transport to the northern part of the EM and Cyprus is modelled with DOD values above 2 and in good spatial agreement with satellite observations. The simulated DOD in this region is less than observed, but one order of magnitude better than other state-of-the-art models, at a longer forecast time and without data assimilation. For the transport to the southern EM, a hydraulic jump is demonstrated to be of crucial importance. It is captured by ICON-ART, albeit with reduced intensity compared to observations. Consequently dust transport into the region is underestimated in the order of one magnitude, with DODs in the range of $0.5 - 1.5$ over Israel and PM10 concentrations up to 600 μg m^{-3} in Jerusalem. Nevertheless, the characteristic dust transport features are captured. The arrival of the main dust plume during the night of 08 September is simulated in 1 km height and subsequent downward mixing increases surface dust concentrations. Again, ICON-ART results are one order of magnitude better than those from other models.

What is the synoptic situation enabling this extreme event and how does it relate to its exceptional character?

The event is enabled by an active RST trough situation. The occurrence of the active RST situation at the beginning of September is unusually early, it thereby explains the extraordinariness of the event with respect to timing. Furthermore, the RST situation enables the interaction of multiple dust emitting meteorological systems over the course of three days, which thereby explains the extraordinariness of the event with respect to magnitude and spatial extent. In particular, the active RST situation enables a period of convectively active days with meso-scale organized convection and associated CPOs. In addition, the formation of an intense heat low above Syria is facilitated. The cyclonic flow around the RST provides the basis for the transport of dust towards southern and westerly directions on its downstream flank which explains the exceptional transport direction of the dust plume into the EM from east.

What are the meteorological drivers responsible for pick-up and long-range transport of mineral dust?

During the early morning hours of 06 September, a sharply defined CPO (CPO1) from an MCS over the Taurus mountain range interacts with a shallow but strong heat low forming in the boundary layer above Syria. Increased dust emissions occur as soon as turbulent mixing of the boundary layer sets in. Subsequently, the flow and dust plume created interact with the EM sea-breeze penetrating land inwards. Downstream of the upper tropospheric trough and with orographic support from the Zagros mountain range, a second MCS develops over the Turkey-Iraq-Iran border region from noon onwards. The MCS rapidly produces a CPO (CPO2) which travels west in the wake of CPO1 and the heat low, again producing substantial dust emission over central Syria. The lifting caused by the gust front of CPO2 triggers initiation of deep convection over the Syria-Iraq border region which organizes into an MCS around 18 UTC. The MCS is again located in a dynamically favourable position downstream the quasi-stationary upper tropospheric trough. It produces another CPO (CPO3) from 20 UTC onwards. CPO3 subsequently counters and lifts the inflow from the Persian Gulf along the RST flank, thereby fuelling the MCS and enabling its sustained lifetime of more than 12 hours. During night-time, the CPO3 gains momentum and spreads towards west. With sunrise and the onset of boundary layer mixing intense dust pick-up occurs in the CPO2 and CPO3 region. During daytime on 07 September, the MCS dissipates. The dust plume connected to CPO3 travels into a south-westerly direction supported by the

Atmos. Chem. Phys. Discuss., doi:10.5194/acp-2017-11, 2017
Manuscript under review for journal Atmos. Chem. Phys.
Published: 3 February 2017

flow on the downstream flank of the RST. The Dead Sea Rift Valley is passed by the merged dust plumes of CPO2 and CPO3 after midnight on 08 September. During the night, the flow interacts with the complex orography. As a result, widespread supercritical flow conditions, and the subsequent hydraulic jumps, occur in the lee of orographic features. This flow phenomena and the related dust emissions add to the extreme dust concentrations in the southern EM on 08 September. During daytime on 08 September, the dust plume is mostly stationary in the EM and influenced by the local circulation systems.

How does the mineral dust radiative effect influence the dust event in general and the evolution of the CPOs in particular?

Besides the feedbacks of the mineral dust radiation interaction which have been identified in the literature before, a previously undocumented effect is found inside the CPO regions. Systematically more intense CPOs and a faster propagation of the CPOs in the mineral dust radiation interaction run are modelled.

Appendix A

A1

Acknowledgements. EUMETSAT and its training group (Jochen Kerkmann, Hans-Peter Roesli and Sancha Lancaster) is gratefully acknowledged for granting the right to use the MSG animation of the dust event. We thank Arnon Karnieli for his effort in establishing and maintaining the Sede Boker AERONET site. The MODIS Aerosol Optical Depth datasets were acquired from the Level-1 Atmosphere Archive and Distribution System (LAADS) Distributed Active Archive Center (DAAC), located in the Goddard Space Flight Center in Greenbelt, Maryland (https://ladsweb.nascom.nasa.gov/). We would like to thank Tami Bond and Christoph Maetzler for making their MatLab based Mie-code publicly available.

Atmos. Chem. Phys. Discuss., doi:10.5194/acp-2017-11, 2017
Manuscript under review for journal Atmos. Chem. Phys.
Published: 3 February 2017

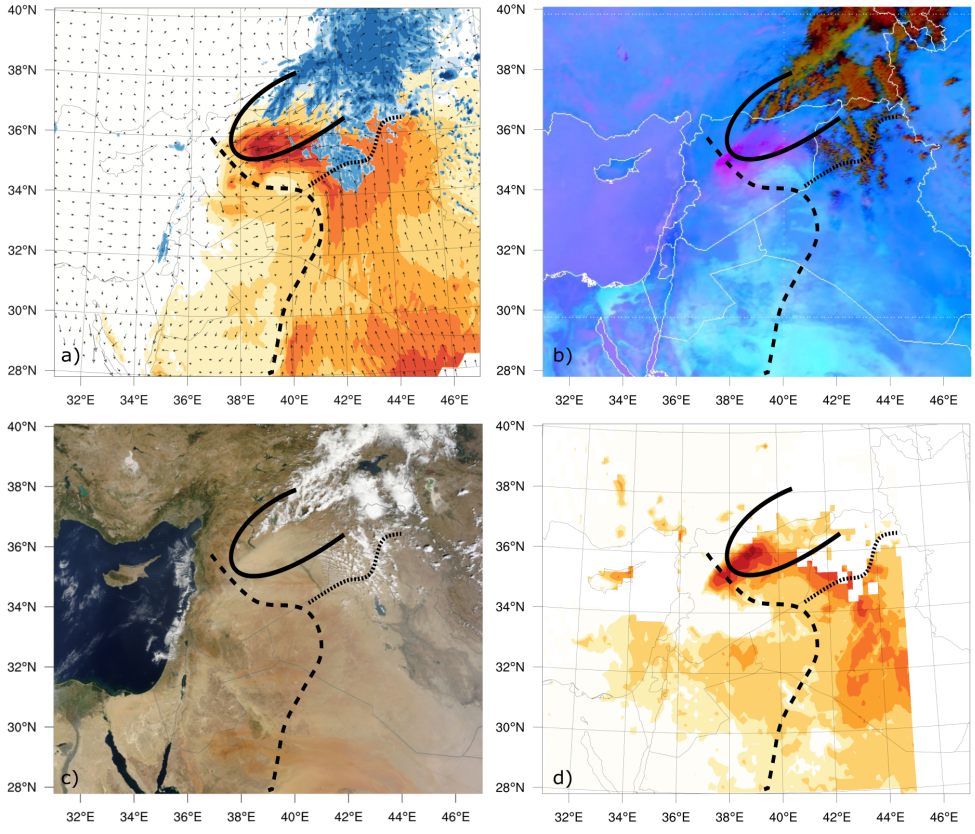

Figure A1. ICON-ART model results and satellite observations at 08 UTC 06 September. Axis for dust optical depths and column integrated hydro-meteor content as in figure 5. Solid black line marks CPO1, dashed black line EM Sea-breeze front from 05 September, dotted black line inflow frontal structure. Displayed are: a) ICON-ART dust optical depth, column integrated hydro-meteor content and wind velocity. b) SEVIRI RGB dust product (Kerkmann et al., 2015). c) Terra MODIS VIS satellite image, overpass at 08.15 UTC (NASA Worldview, 2016). d) Terra MODIS dust optical depth retrieval using DB2 algorithm (AOD-0.3) (Levy and Hsu, 2015), overpass at 08.15 UTC.

Atmos. Chem. Phys. Discuss., doi:10.5194/acp-2017-11, 2017
Manuscript under review for journal Atmos. Chem. Phys.
Published: 3 February 2017

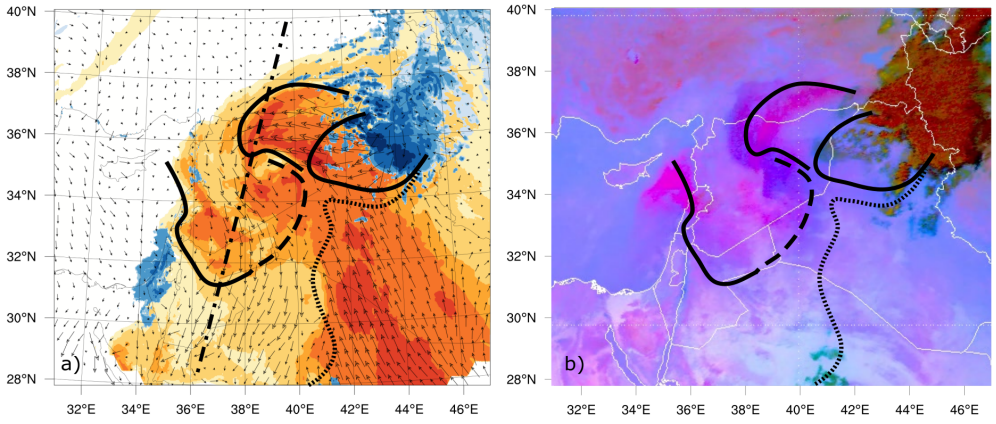

Figure A2. ICON-ART model results and EUMETSAT satellite observations at 00 UTC 07 September. From west to east solid black mark leading edges of CPO1, CPO2 and CPO3. Dashed line marks EM Sea-breeze front from 06 September. Dotted line marks frontal region of inflow. Chain dotted black line marks CALIPSO ground track at 23.35 UTC 06 September. Left side: ICON-ART dust optical depth, column integrated hydro-meteor content and wind velocity. Right side: SEVIRI RGB dust product.

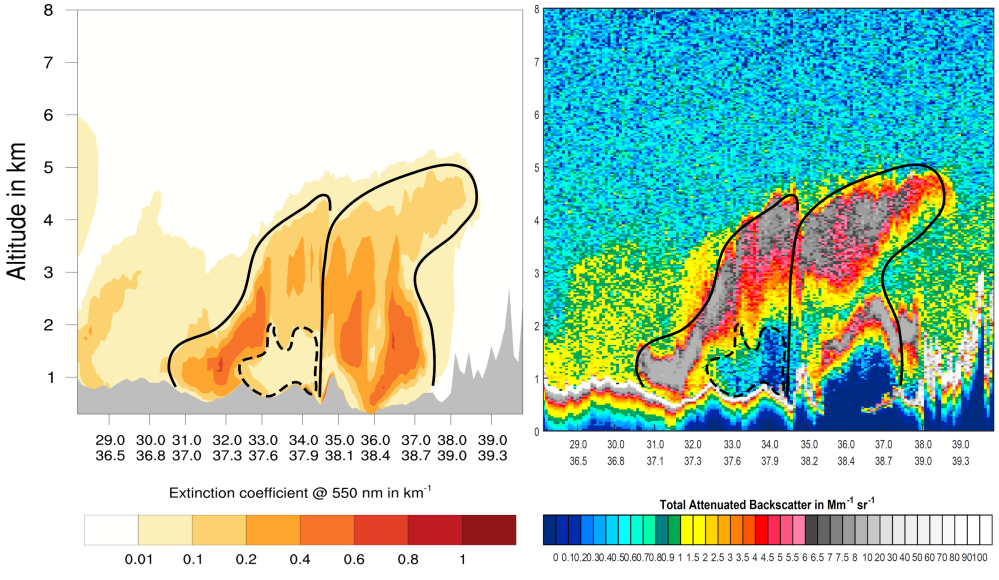

Figure A3. Vertical cross-section of ICON-ART model results at 00 UTC 07 September and CALIPSO satellite observations from south to north along ground track in figure A2. Left side: ICON-ART mineral dust extinction coefficient. Right side: Total attenuated backscatter as measured by CALIOP. No quantitative comparison is possible as two different measures are displayed. Southern solid black line marks CPO1 and HL region. Dashed line marks penetrating EM Sea-breeze. Northern solid black line marks CPO2 region.

Atmos. Chem. Phys. Discuss., doi:10.5194/acp-2017-11, 2017
Manuscript under review for journal Atmos. Chem. Phys.
Published: 3 February 2017

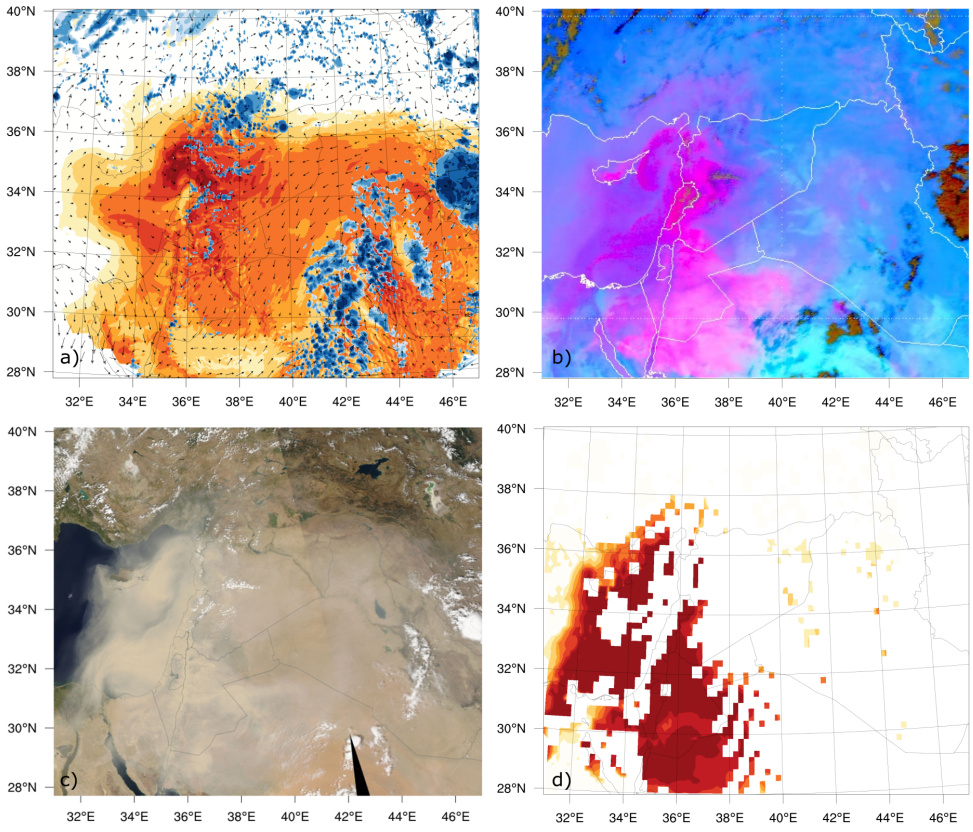

Figure A4. ICON-ART model results and satellite observations at 11 UTC 08 September. Same as figure A1 but for Aqua MODIS instrument, overpass for the left part of the picture at 11.18 UTC. Please note that in this case the MODIS Dark Target and Deep Blue combined AOD product is displayed in order to obtain values over sea.

References

Alpert, P., Osetinsky, I., Ziv, B., and Shafir, H.: A new seasons definition based on classified daily synoptic systems: an example for the eastern Mediterranean, Int. J. Climatol., 24, 1013–1021, 2004.

Alpert, P., Egert, S., and Uzan, L.: The 7-13 September extreme dust downfall over the East Mediterranean A two ceilometers study, in: EGU General Assembly Conference Abstracts, vol. 18, p. 3788, 2016.

Arino, O., Bicheron, P., Achard, F., Latham, J., Witt, R., and Weber, J.-L.: The most detailed portrait of Earth, European Space Agency Bull, 136, 25–31, 2008.

Bangert, M., Nenes, A., Vogel, B., Vogel, H., Barahona, D., Karydis, V. A., Kumar, P., Kottmeier, C., and Blahak, U.: Saharan dust event impacts on cloud formation and radiation over Western Europe, Atmos. Chem. Phys., 12, 4045–4063, doi:10.5194/acp-12-4045-2012, 2012.

Bitan, A. and Sa'Aroni, H.: The horizontal and vertical extension of the Persian Gulf pressure trough, Int. J. Climatol., 12, 733–747, 1992.

Bohren, C. F. and Huffman, D. R.: Absorption and scattering of light by small particles, Wiley -VCH, Weinheim, Germany, repr. 2004 edn., doi:10.1002/9783527618156, 1983.

Bond, T. C., Habib, G., and Bergstrom, R. W.: Limitations in the enhancement of visible light absorption due to mixing state, J. Geophys. Res.-Atmos., 111, D20211, 1–13, 2006.

Boucher, O., Randall, D., Artaxo, P., Bretherton, C., Feingold, G., Forster, P., Kerminen, V.-M., Kondo, Y., Liao, H., Lohmann, U., et al.: Clouds and Aerosols, in: The Physical Science Basis. Contribution of Working Group I to the Fifth Assessment Report of the Intergovernmental Panel on Climate Change, pp. 571–657, Cambridge University Press, Cambridge, United Kingdom and New York, NY, USA, 2013.

Carslaw, K., Boucher, O., Spracklen, D., Mann, G., Rae, J., Woodward, S., and Kulmala, M.: A review of natural aerosol interactions and feedbacks within the Earth system, Atmos. Chem. Phys., 10, 1701–1737, 2010.

Cuesta, J., Marsham, J. H., Parker, D. J., and Flamant, C.: Dynamical mechanisms controlling the vertical redistribution of dust and the thermodynamic structure of the West Saharan atmospheric boundary layer during summer, Atmos. Sci. Lett., 10, 34–42, 2009.

Dayan, U., Heffter, J., Miller, J., and Gutman, G.: Dust intrusion events into the Mediterranean basin, Journal of Applied Meteorology, 30, 1185–1199, 1991.

Dayan, U., Ziv, B., Shoob, T., and Enzel, Y.: Suspended dust over southeastern Mediterranean and its relation to atmospheric circulations, Int. J. Climatol., 28, 915–924, 2008.

Drobinski, P., Flamant, C., Dusek, J., Flamant, P. H., and Pelon, J.: Observational Evidence And Modelling Of An Internal Hydraulic Jump At The Atmospheric Boundary-Layer Top During A Tramontane Event, Boundary Layer Meteorol., 3, 497–515, 2001.

Drobinski, P., Bastin, S., Janicot, S., Bock, O., Dabas, A., Delville, P., Reitebuch, O., and Sultan, B.: On the late northward propagation of the West African monsoon in summer 2006 in the region of Niger/Mali, J. Geophys. Res.-Atmos., 114, D09108, 1–16, 2009.

Fécan, F., Marticorena, B., and Bergametti, G.: Parametrization of the increase of the aeolian erosion threshold wind friction velocity due to soil moisture for arid and semi-arid areas, Ann. Geophys., 17, 149–157, doi:10.1007/s00585-999-0149-7, 1999.

Ganor, E.: The composition of clay minerals transported to Israel as indicators of Saharan dust emission, Atmospheric Environment. Part A. General Topics, 25, 2657–2664, 1991.

Gasch, P.: Numerical simulations of an exceptional dust event in the Eastern Mediterranean including the mineral dust radiative feedback, Master's thesis, Karlsruhe Institute of Technology, 1–125, 2016.

Gleick, P. H.: Water, drought, climate change, and conflict in Syria, Weather, Climate, and Society, 6, 331–340, 2014.

Heinold, B., Tegen, I., Schepanski, K., and Hellmuth, O.: Dust radiative feedback on Saharan boundary layer dynamics and dust mobilization, Geophys. Res. Lett., 35, L20817, 1–5, 2008.

Heinold, B., Knippertz, P., Marsham, J., Fiedler, S., Dixon, N., Schepanski, K., Laurent, B., and Tegen, I.: The role of deep convection and nocturnal low-level jets for dust emission in summertime West Africa: Estimates from convection-permitting simulations, J. Geophys. Res.-Atmos., 118, 4385–4400, 2013.

Helmert, J., Heinold, B., Tegen, I., Hellmuth, O., and Wendisch, M.: On the direct and semidirect effects of Saharan dust over Europe: A modeling study, J. Geophys. Res.-Atmos., 112, D13208, 1–24, 2007.

Highwood, E. J. and Ryder, C. L.: Dust Production Mechanisms, in: Mineral Dust, edited by Knippertz, P. and Stuut, J.-B. W., chap. 11, pp. 267–286, Springer, Dordrecht, Netherlands, 2014.

Kahnert, M., Nousiainen, T., and Räisänen, P.: Mie simulations as an error source in mineral aerosol radiative forcing calculations, Quart. J. Roy. Meteor. Soc., 133, 299–307, 2007.

Kalenderski, S. and Stenchikov, G.: High-resolution regional modeling of summertime transport and impact of African dust over the Red Sea and Arabian Peninsula, J. Geophys. Res.-Atmos., 121, 6435 – 6458, 2016.

Kerkmann, J., Lancaster, S., and Roesli, H. P.: Many parts of the Middle East were shrouded in a persistent dust cloud in early September., URL http://www.eumetsat.int/website/home/Images/ImageLibrary/DAT_2773503.html, last accessed 08 Aug 2016, 2015.

Kishcha, P., Rieger, D., Metzger, J., Starobinets, B., Bangert, M., Vogel, H., Schättler, U., Corsmeier, U., Alpert, P., and Vogel, B.: Modelling of a strong dust event in the complex terrain of the Dead Sea valley during the passage of a gust front, Tellus B, 68, 29751, 1–19, 2016.

Knippertz, P.: Meteorological aspects of dust storms, in: Mineral Dust, edited by Knippertz, P. and Stuut, J.-B. W., chap. 6, pp. 121–147, Springer, Dordrecht, Netherlands, 2014.

Knippertz, P., Deutscher, C., Kandler, K., Müller, T., Schulz, O., and Schütz, L.: Dust mobilization due to density currents in the Atlas region: Observations from the Saharan Mineral Dust Experiment 2006 field campaign, J. Geophys. Res.-Atmos., 112, D21109, 1–14, 2007.

Krichak, S. O., Breitgand, J. S., and Feldstein, S. B.: A conceptual model for the identification of active Red Sea trough synoptic events over the southeastern Mediterranean, J. of Applied Met. and Clim., 51, 962–971, 2012.

Kubilay, N., Nickovic, S., Moulin, C., and Dulac, F.: An illustration of the transport and deposition of mineral dust onto the eastern Mediterranean, Atmospheric Environment, 34, 1293–1303, 2000.

Levi, Y. and Rosenfeld, D.: Ice nuclei, rainwater chemical composition, and static cloud seeding effects in Israel, Journal of Applied Meteorology, 35, 1494–1501, 1996.

Levy, R. and Hsu, C.: MODIS Atmosphere L2 Aerosol Product, Tech. rep., NASA, Goddard Space Flight Center, USA, doi:10.5067/MODIS/MOD04_L2.006, 2015.

Mamouri, R.-E., Nisantzi, A., Ansmann, A., and Hadjimitsis, D. G.: Extreme dust storm over the eastern Mediterranean in September 2015: Lidar vertical profiling of desert dust at Limassol, Cyprus, Atmos. Chem. Phys. Discuss., 2016, 1–12, doi:10.5194/acp-2016-354, 2016.

Marsham, J. H., Knippertz, P., Dixon, N. S., Parker, D. J., and Lister, G.: The importance of the representation of deep convection for modeled dust-generating winds over West Africa during summer, Geophys. Res. Lett., 38, L16803, 1–6, 2011.

Mätzler, C.: MATLAB functions for Mie scattering and absorption, version 2, Tech. rep., Institute of Applied Physics, University of Bern, 1–26, 2002.

Metzger, J.: Wind Systems and Energy Balance in the Dead Sea Valley, Ph.D. thesis, Karlsruhe Institute of Technology, Karlsruhe, 2016.

Miller, S. D., Kuciauskas, A. P., Liu, M., Ji, Q., Reid, J. S., Breed, D. W., Walker, A. L., and Mandoos, A. A.: Haboob dust storms of the southern Arabian Peninsula, J. Geophys. Res.-Atmos., 113, D01202, 1–26, 2008.

Mishchenko, M., Lacis, A., Carlson, B., and Travis, L.: Nonsphericity of dust-like tropospheric aerosols: Implications for aerosol remote sensing and climate modeling, Geophys. Res. Lett., 22, 1077–1080, 1995.

Mishchenko, M. I., Travis, L. D., Kahn, R. A., and West, R. A.: Modeling phase functions for dustlike tropospheric aerosols using a shape mixture of randomly oriented polydisperse spheroids, J. Geophys. Res.-Atmos., 102, 16 831–16 847, 1997.

Mlawer, E. J., Taubman, S. J., Brown, P. D., Iacono, M. J., and Clough, S. A.: Radiative transfer for inhomogeneous atmospheres: RRTM, a validated correlated-k model for the longwave, J. Geophys. Res.-Atmos., 102, 16 663–16 682, 1997.

Nachtergaele, F. and Batjes, N.: Harmonized world soil database, Food and Agriculture Organization of the United Nations, Rome, 1–35, 2012.

NASA Earth Observatory: Dust Storm Sweeps Across Middle East, URL http://earthobservatory.nasa.gov/NaturalHazards/view.php?id=86571, last accessed 25 Aug 2016, 2015.

NASA Worldview: URL https://worldview.earthdata.nasa.gov/, last accessed 08 Aug 2016, 2016.

Notaro, M., Yu, Y., and Kalashnikova, O. V.: Regime shift in Arabian dust activity, triggered by persistent Fertile Crescent drought, Journal of Geophysical Research: Atmospheres, 120, 2015.

Offer, Z. Y. and Goossens, D.: Ten years of aeolian dust dynamics in a desert region (Negev desert, Israel): analysis of airborne dust concentration, dust accumulation and the high-magnitude dust events, Journal of Arid Environments, 47, 211–249, 2001.

Osetinsky, I.: Climate changes over the E. Mediterranean - A synoptic systems classification approach, Ph.D. thesis, Tel Aviv University, Tel Aviv, 2006.

Otto, S., Bierwirth, E., Weinzierl, B., Kandler, K., Esselborn, M., Tesche, M., Schladitz, A., Wendisch, M., and Trautmann, T.: Solar radiative effects of a Saharan dust plume observed during SAMUM assuming spheroidal model particles, Tellus B, 61, 270–296, 2009.

Pérez, C., Nickovic, S., Pejanovic, G., Baldasano, J. M., and Özsoy, E.: Interactive dust-radiation modeling: A step to improve weather forecasts, J. Geophys. Res.-Atmos., 111, D16206, 1–17, 2006.

Petty, G. W.: A first course in atmospheric radiation, Sundog Pub, Madison, USA, 2006.

Raupach, M. et al.: Dry deposition of gases and particles to vegetation, Clean Air: Journal of the Clean Air Society of Australia and New Zealand, 27, 200–203, 1993.

Redl, R., Knippertz, P., and Fink, A. H.: Weakening and moistening of the summertime Saharan heat low through convective cold pools from the Atlas Mountains, J. Geophys. Res.-Atmos., 121, 3907–3928, 2016.

Rémy, S., Benedetti, A., Bozzo, A., Haiden, T., Jones, L., Razinger, M., Flemming, J., Engelen, R., Peuch, V., and Thepaut, J.: Feedbacks of dust and boundary layer meteorology during a dust storm in the eastern Mediterranean, Atmos. Chem. Phys., 15, 12 909–12 933, 2015.

Rieger, D.: Der Einfluss von natürlichem Aerosol auf Wolken, Ph.D. thesis, Karlsruhe Institute of Technology, Karlsruhe, 2016.

Rieger, D., Bangert, M., Bischoff-Gauss, I., Förstner, J., Lundgren, K., Reinert, D., Schröter, J., Vogel, H., Zängl, G., Ruhnke, R., et al.: ICON–ART 1.0–a new online-coupled model system from the global to regional scale, Geosci. Model Dev., 8, 1659–1676, 2015.

Seifert, A. and Beheng, K.: A two-moment cloud microphysics parameterization for mixed-phase clouds. Part 1: Model description, Meteorol. Atmos. Phys., 92, 45–66, 2006.

Seifert, A. and Beheng, K. D.: A double-moment parameterization for simulating autoconversion, accretion and selfcollection, Atmos. Res., 59, 265–281, 2001.

Shao, Y. and Lu, H.: A simple expression for wind erosion threshold friction velocity, J. Geophys. Res.-Atmos., 105, 22 437–22 443, 2000.

Shao, Y., Wyrwoll, K.-H., Chappell, A., Huang, J., Lin, Z., McTainsh, G. H., Mikami, M., Tanaka, T. Y., Wang, X., and Yoon, S.: Dust cycle: An emerging core theme in Earth system science, Aeolian Res., 2, 181–204, doi:http://dx.doi.org/10.1016/j.aeolia.2011.02.001, 2011a.

Singer, A., Ganor, E., Dultz, S., and Fischer, W.: Dust deposition over the Dead Sea, J. Arid. Environ., 53, 41–59, 2003.

Solomos, S., Ansmann, A., Mamouri, R.-E., Binietoglou, I., Patlakas, P., Marinou, E., and Amiridis, V.: Remote sensing and modeling analysis of the extreme dust storm hitting Middle East and Eastern Mediterranean in September 2015, Atmospheric Chemistry and Physics Discussions, 2016, 1–31, doi:10.5194/acp-2016-1006, 2016.

Spyrou, C., Kallos, G., Mitsakou, C., Athanasiadis, P., Kalogeri, C., and Iacono, M.: Modeling the radiative effects of desert dust on weather and regional climate, Atmos. Chem. Phys., 13, 5489–5504, 2013.

Stanelle, T., Vogel, B., Vogel, H., Bäumer, D., and Kottmeier, C.: Feedback between dust particles and atmospheric processes over West Africa during dust episodes in March 2006 and June 2007, Atmos. Chem. Phys., 10, 10 771–10 788, 2010.

Tegen, I. and Lacis, A. A.: Modeling of particle size distribution and its influence on the radiative properties of mineral dust aerosol, J. Geophys. Res.-Atmos., 101, 19 237–19 244, 1996.

Tegen, I., Heinold, B., Todd, M., Helmert, J., Washington, R., and Dubovik, O.: Modelling soil dust aerosol in the Bodélé depression during the BoDEx campaign, Atmos. Chem. Phys., 6, 4345–4359, 2006.

The Weather Channel: Intense Middle East Dust Storm Kills At Least 5, Sickens Hundreds, URL https://weather.com/news/news/severe-middle-east-sandstorm - dust-storm-jordan-israel-lebanon-syria-iraq, last accessed 08 Aug 2016, 2015.

Times Of Israel: Heavy dust blankets country for second day as intense heat joins in, URL http://www.timesofisrael.com/heavy-dust-to-blanket-country-for-second-day-as-intense-heat-joins-in/, last accessed 25 Aug 2016, 2015.

Tsvieli, Y. and Zangvil, A.: Synoptic climatological analysis of wet and dry Red Sea troughs over Israel, Int. J. Climatol., 25, 1997–2015, 2005.

Vogel, B., Hoose, C., Vogel, H., and Kottmeier, C.: A model of dust transport applied to the Dead Sea area, Meteorol. Z., 15, 611–624, 2006.

Voss, K. A., Famiglietti, J. S., Lo, M., Linage, C., Rodell, M., and Swenson, S. C.: Groundwater depletion in the Middle East from GRACE with implications for transboundary water management in the Tigris-Euphrates-Western Iran region, Water resources research, 49, 904–914, 2013.

Vries, A., Tyrlis, E., Edry, D., Krichak, S., Steil, B., and Lelieveld, J.: Extreme precipitation events in the Middle East: dynamics of the Active Red Sea Trough, J. Geophys. Res.-Atmos., 118, 7087–7108, 2013.

Wagner, R., Ajtai, T., Kandler, K., Lieke, K., Linke, C., Müller, T., Schnaiter, M., and Vragel, M.: Complex refractive indices of Saharan dust samples at visible and near UV wavelengths: a laboratory study, Atmospheric Chemistry and Physics, 12, 2491–2512, doi:10.5194/acp-12-2491-2012, http://www.atmos-chem-phys.net/12/2491/2012/, 2012.

Zängl, G., Reinert, D., Rípodas, P., and Baldauf, M.: The ICON (ICOsahedral Non-hydrostatic) modelling framework of DWD and MPI-M: Description of the non-hydrostatic dynamical core, Quart. J. Roy. Meteor. Soc., 141, 563–579, 2015.